Spin diffusion induced by pulsed-laser heating and the role of spin heat accumulation

Johannes Kimling* and David G. Cahill

Department of Materials Science and Engineering and Materials Research Laboratory, University of Illinois, Urbana, Illinois 61801, USA

(Received 25 May 2016; revised manuscript received 14 October 2016; published 3 January 2017)

We present a model for describing spin diffusion in normal-metal/ferromagnetic-metal heterostructures induced by pulsed-laser heating. The model is based on the assumptions that electronic heat currents give rise to the spin-dependent Seebeck effect and that ultrafast demagnetization generates spin accumulation with a rate proportional to the demagnetization rate measured. Spin-diffusion currents are then driven by gradients in spin accumulation and electron temperature. The model considers spin-dependent thermal conductivity and electron-phonon coupling, which can give rise to different effective temperatures for majority and minority spins, known as spin heat accumulation. We find that spin heat accumulation can significantly enhance the spin-dependent Seebeck effect.

DOI: 10.1103/PhysRevB.95.014402

I. INTRODUCTION

Recent developments in the field of spintronics promise new methods for the generation of spin currents [1]. Spin transport caused by laser excitation of thin films composed of ferromagnetic-metal and normal-metal layers has been reported in a number of pump-probe experiments [2–10]. In Refs. [3–7], direct interaction of laser light with the ferromagnetic layers is assumed to cause superdiffusive spin transport (SDST) based on different lifetimes and velocities of majority and minority spins in high-energy states [11].

The experimental results of SDST are in qualitative agreement with the SDST theory. A quantitative demarcation from spin diffusion has been achieved by Melnikov *et al.*, who study spin transport in Fe/Au bilayers, induced by 35 fs laser pulses and detected at the Au surface using optical second harmonic generation [3]. By varying the Au layer thickness, Melnikov *et al.* find a spin signal that propagates in Au with a velocity close to the group velocity of electrons.

An alternative approach has been reported by Choi *et al.*, who use indirect excitation of a ferromagnetic metal placed between a Pt transducer and a Cu heat sink with picosecond laser pulses. This approach allows for sizable electronic heat currents of the order of 100 GW m^{-2} [9,10]. Choi *et al.* assume that the heat current results in ultrafast demagnetization of the ferromagnetic layer and gives rise to the spin-dependent Seebeck effect (SDSE). Choi *et al.* state "...we showed that the demagnetization-driven spin generation is due to electron-magnon coupling..." [9,10]. This statement is too strong for two reasons. First, Choi *et al.* find that their experimental data can be explained assuming that the spin chemical potential of the ferromagnetic layer changes proportionally to the time derivative of the magnetization of the ferromagnetic layer, probed by the time-resolved magneto-optic Kerr effect (TRMOKE). This assumption does not necessarily imply electron-magnon coupling. Second, assignment of a strong degree of certainty to a hypothesis is unnecessary and misleading because the agreement between a model prediction and a measurement can only corroborate the assumptions of the model. Nevertheless, Choi *et al.* achieve quantitative agreement between model prediction and measurement considering conventional heat- and spin-diffusion equations [9,10,12]. Moreover, by varying the Cu layer thickness, Choi *et al.* find a spin signal that propagates with a velocity that is more than one order of magnitude smaller than the group velocity of electrons.

Spin-dependent thermal transport through interfaces with a ferromagnetic metal can cause different effective temperatures for majority and minority spins, known as spin heat accumulation (SHA) [13–16]. Prior research on the SDSE assumed local thermal equilibrium between majority and minority spins, i.e., neglected possible influences of SHA on thermally driven spin currents [10,17,18].

Here, we present a heat- and spin-diffusion model for describing spin transport in nanoscale metal layers induced by pulsed-laser heating that considers different effective temperatures for majority and minority spins (Sec. III). We introduce three approximations that yield to a simplified spin-diffusion model that has been used without further justification by Choi *et al.* (Sec. IV) [10]. We argue that the approximation of zero SHA is not generally valid and analyze the influence of SHA on the SDSE (Sec. V). Since we find that SHA can significantly influence the SDSE, we discuss the material parameters required for increasing the SDSE through SHA (Sec. VI A).

II. PROBLEM SITUATION

Consider a metal stack composed of a 20 nm Pt transducer, a 3 nm ferromagnetic metal (FM1), and a 100 nm Cu heat sink, as studied by Choi *et al.* [10] and illustrated in Fig. 1. The multilayered materials that Choi *et al.* chose for FM1 are $[Co(0.2)/Pt(0.4)]_{\times 5}/Co(0.2)$ and $[Co(0.2)/Ni(0.4)]_{\times 5}/Co(0.2)$ with perpendicular magnetic anisotropy. The metal stack is situated on a sapphire substrate (starting with the Pt layer) and capped with 10 nm MgO and 5 nm Al_2O_3. Laser excitation of the Pt transducer through the sapphire substrate can initiate spin transport. Choi *et al.* measure spin transport in two experiments: In what we call Experiment I, the spin current induces a precession of a second ferromagnetic layer (FM2) attached at the Cu end with in-plane magnetization [Fig. 1(a)]; in Experiment II, the spin current creates spin accumulation in the Cu layer [Fig. 1(b)]. Both phenomena have been measured using TRMOKE [9,10].

*kimling@illinois.edu

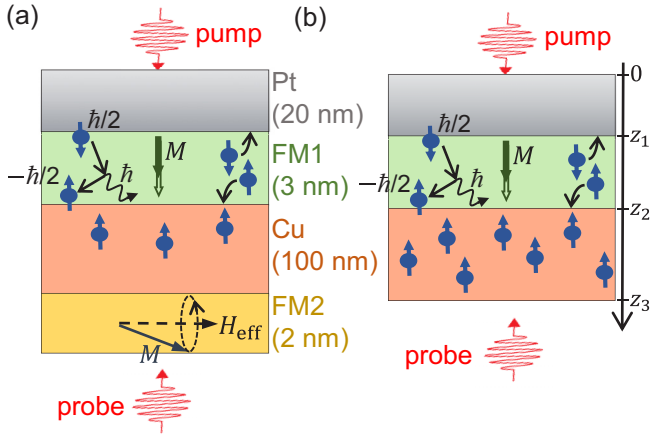

FIG. 1. Conceptual diagrams of possible spin-generation mechanisms and of the detection approaches used in the two experiments studied. Laser excitation creates spin accumulation in FM1 via electron-magnon scattering and spin-dependent Seebeck effect. Resulting spin signals are detected at the opposite side of the sample using time-resolved magneto-optic Kerr effect. (a) Experiment I probes magnetization precession of FM2 induced by thermal spin-transfer torque; (b) Experiment II probes spin accumulation injected into the Cu layer [10]. Substrate and capping layers are not shown in the schematics. The metal stack is deposited on a sapphire substrate starting with the Pt layer; the top metal layer is capped with 10 nm MgO and 5 nm Al_2O_3.

As determined using a transfer matrix optical model, approximately 99% of the total absorbed near-infrared laser light (wavelength 785 nm) is absorbed in the Pt/FM1 bilayer (Appendix B). The photon energy of ∼1.6 eV absorbed by electrons initially creates a nonthermal electron distribution that thermalizes to a Fermi-Dirac distribution via inelastic scatterings. Time-resolved photoemission spectroscopy indicates that complete electron thermalization is achieved after ∼1 ps in Au and after ∼0.5 ps in Ni [19,20]. The excited electrons transfer energy to the lattice through excitation of phonons and magnons. The thermalization time of electrons and phonons in Pt, $\tau_{ep} = C_e/g_{ep} \approx 0.8$ ps (Table II), is comparable to the duration of pump pulses in the experiments considered here.

By presupposing that the individual layers are thicker than the respective mean free paths of electrons, the electron thermalization process is accompanied by fast electronic heat transport, which undergoes different stages from ballistic transport, for time scales shorter than the lifetime of electrons (∼10 fs) [21], to superdiffusive transport, for time scales shorter than the electron thermalization time, to diffusive transport after electron thermalization [11,22].

Before thermalization of electrons with the lattice, high electron temperatures locally confined to the Pt layer result in a sizable heat current through layer FM1 into the Cu heat sink. Due to the dominating heat capacity of phonons, cooling of electrons to the phonon temperature significantly reduces the heat current, which persists until Pt and Cu layers are in thermal equilibrium. Assuming an interface thermal conductance of $G = 100\,\mathrm{MW\,m^{-2}\,K^{-1}}$, the characteristic time for heat to cross the Pt/sapphire interface is $h_{tot}C_{tot}/G \approx 4$ ns. Therefore, only a small amount of heat is transported across the Pt/sapphire interface during equilibration of the metal stack.

III. MODEL

We assume that the heat current through layer FM1 gives rise to two spin sources, i.e., SDSE and ultrafast demagnetization, elaborated in Secs. III A and III B. We further assume that the heat and spin transport is dominated by diffusion, i.e., can be described using heat- and spin-diffusion equations derived in Secs. III C and III D. This approximation is reasonable since the duration of laser pulses is longer than the thermalization time of electrons to a Fermi-Dirac distribution and since the thicknesses of the individual layers are larger than the respective electron mean free paths (in Sec. V and Appendix A 3, we obtain a small spin-relaxation time of layer FM1, which implies that even for the only 3-nm-thick layer FM1, the mean free path is smaller than the layer thickness). The boundary conditions of the model are described in Sec. III E.

A. Spin-dependent Seebeck effect and spin heat accumulation

Finite temperature broadens the Fermi-Dirac distribution at the Fermi energy. In the presence of a temperature gradient in the z direction, the broadening becomes a function of z. As a consequence, hot electrons above the Fermi energy and cold electrons below the Fermi energy diffuse in opposite directions. In general, there is an imbalance, i.e., a net charge current occurs that can generate a thermoelectric voltage in an open circuit. This phenomenon is known as the Seebeck effect.

The spin-polarized band structure of a ferromagnetic metal gives rise to different Seebeck coefficients for majority and minority spins. As a result, a temperature gradient can drive a spin current that generates spin accumulation of opposite signs at the edges of the ferromagnet. This phenomenon is known as the spin-dependent Seebeck effect (SDSE) [23].

If a heat current flows from a ferromagnetic metal into a normal metal, the asymmetry of the heat currents carried by majority- and minority-spin electrons changes from a finite value in the ferromagnetic metal to zero in the normal metal. As a consequence, there is a mismatch in the distribution functions of majority and minority spins on a length scale $l_{SHA} \approx \sqrt{D\tau_{S,th}}$ from the interface, determined by the diffusion constant of electrons, D, and the thermalization time between majority and minority spin electrons, $\tau_{S,th}$. If the individual thermalization times of majority and minority spins are comparable to $\tau_{S,th}$, then majority and minority spins cannot be described by Fermi-Dirac distribution functions at distances shorter than $l_{S,th}$ from normal-metal/ferromagnetic-metal (NM/FM) interfaces. However, according to Ref. [14], it is possible to assume Fermi-Dirac distribution functions after defining effective electron temperatures and chemical potentials. The difference between the two effective electron temperatures, $T_\uparrow - T_\downarrow$, is then a measure of the difference of the heat stored in the majority-spin electrons and the heat stored in the minority-spin electrons. Spin heat accumulation is a transport effect, which persists even in steady state.

Laser heating of the Pt transducer creates temperature gradients $\partial T_\uparrow/\partial z$ and $\partial T_\downarrow/\partial z$ in FM1, which leads to spin diffusion into the adjacent Pt and Cu layers.

B. Spin generation by ultrafast demagnetization

During laser excitation of the Pt transducer, fast electronic heat transport through the Pt/FM1 interface causes ultrafast demagnetization of FM1 [9,10]. A discussion of possible mechanisms of ultrafast demagnetization can be found in Ref. [24]. We assume that ultrafast de- and remagnetization generates spin accumulation in the conduction electrons of FM1,

$$\mu_{\mathrm{B}}\frac{\partial(n_{\uparrow}-n_{\downarrow})}{\partial t}=-\frac{\partial M}{\partial t}, \tag{1}$$

where $n_{\uparrow}$ and $n_{\downarrow}$ are number densities of majority and minority spins, μ_{B} is the Bohr magneton, and $\frac{\partial M}{\partial t}$ is the time derivative of the magnetization M determined using TRMOKE. A possible mechanism that could explain Eq. (1) is the exchange interaction that gives rise to electron-magnon scattering, transferring angular momentum from $3d$ electrons of the magnetic system to $4s$ electrons that dominate the conductivity. If the total angular momentum of the electrons during electron-magnon scattering is conserved, changes in M are directly converted into spin accumulation in the $4s$ electrons. Generation of spin accumulation is accompanied by spin relaxation, e.g., via spin-orbit interaction giving rise to incoherent spin-flip processes that transfer angular momentum from electrons to the lattice.

The above hypothesis of electron-magnon scattering requires either that the sensitivity of TRMOKE to the magnetization in the $4s$ electrons is small compared to the magnetization in the $3d$ electrons or that the relaxation of the spin accumulation and/or the spin transport into adjacent layers occur on a time scale that is short compared to the time resolution of the measurement. In the latter case, the magnetization present in the $4s$ electrons is small compared to the magnetization of the $3d$ electrons at each relevant time step of the measurement.

In any case, spin accumulation created during ultrafast demagnetization of FM1 drives a spin-diffusion current into the adjacent Pt and Cu layers.

C. Currents

Based on the two-current model of ferromagnetic transition metals [25], we consider electronic transport of charge and heat by two coupled transport channels of majority and minority spins, driven by gradients in spin-dependent electrochemical potentials and temperatures [26]. In metals, thermal transport is dominated by electrons. At room temperature, phonons provide an additional thermal transport channel with dominating heat capacity that is coupled to electrons via electron-phonon scattering. We neglect the heat capacity of the thermodynamic reservoir of magnons, which becomes significant near the Curie temperature [27].

In linear response, electrical and thermal current densities, j and q, considered here are given by [23]

$$j_s=\frac{\sigma_s}{e}\frac{\partial\Phi_s}{\partial z}-S_s\sigma_s\frac{\partial T_s}{\partial z}, \tag{2}$$

$$q_s=-\Lambda_s\frac{\partial T_s}{\partial z}+\frac{S_s\sigma_s T_s}{e}\frac{\partial\Phi_s}{\partial z}, \tag{3}$$

$$q_{\mathrm{p}}=-\Lambda_{\mathrm{p}}\frac{\partial T_{\mathrm{p}}}{\partial z}, \tag{4}$$

where subscript p refers to phonons, $s=\uparrow$ for majority spins, and $s=\downarrow$ for minority spins; σ and Λ denote electrical and thermal conductivities, S denotes the Seebeck coefficient, Φ denotes electrochemical potential, and T denotes temperature; e is the elementary charge. The electrochemical potential $\Phi_s=-e\varphi+\zeta_s$ comprises electric potential φ and chemical potential ζ_s.

In the following, we neglect the Peltier term in Eq. (3), which is a good approximation in metals, since $S^2\ll L$, where L is the Lorenz number. In that case, heat transport can be considered independently from charge transport. Furthermore, we assume that the magnetization vector is uniform in space and parallel to the effective magnetic field.

D. Transport equations

Charge carrier number density $n=n_{\uparrow}+n_{\downarrow}$ and electrical current density $j=j_{\uparrow}+j_{\downarrow}$ are connected by the continuity equation

$$-e\frac{\partial n}{\partial t}+\frac{\partial j}{\partial z}=0. \tag{5}$$

By presupposing the electron temperature remains well below the Fermi temperature, the Sommerfeld approximation of $n_{\uparrow}$ yields

$$\frac{\partial n_{\uparrow}}{\partial t}=\frac{\partial n_{\uparrow}}{\partial\zeta_{\uparrow}}\frac{\partial\zeta_{\uparrow}}{\partial t}\approx N_{\uparrow}\frac{\partial\zeta_{\uparrow}}{\partial t}, \tag{6}$$

where $N_{\uparrow}$ is the density of states of majority spins at the Fermi energy (the equivalent equation holds for $n_{\downarrow}$). Using Eqs. (2) and (6), Eq. (5) can be separated into [28]

$$\frac{\partial\zeta_{\uparrow}}{\partial t}+D_{\uparrow}\left(e\frac{\partial^2\varphi}{\partial z^2}-\frac{\partial^2\zeta_{\uparrow}}{\partial z^2}+eS_{\uparrow}\frac{\partial^2 T_{\uparrow}}{\partial z^2}\right)=\frac{-\alpha}{eN_{\uparrow}}(\zeta_{\uparrow}-\zeta_{\downarrow})+\left(\frac{\partial\zeta_{\uparrow}}{\partial t}\right)_{\mathrm{S}}, \tag{7}$$

$$\frac{\partial\zeta_{\downarrow}}{\partial t}+D_{\downarrow}\left(e\frac{\partial^2\varphi}{\partial z^2}-\frac{\partial^2\zeta_{\downarrow}}{\partial z^2}+eS_{\downarrow}\frac{\partial^2 T_{\downarrow}}{\partial z^2}\right)=\frac{\alpha}{eN_{\downarrow}}(\zeta_{\uparrow}-\zeta_{\downarrow})+\left(\frac{\partial\zeta_{\downarrow}}{\partial t}\right)_{\mathrm{S}}, \tag{8}$$

where $D_s=\frac{\sigma_s}{e^2N_s(E_{\mathrm{F}})}$ is the spin-dependent diffusion constant, and α can be related to the spin-relaxation time τ_{S} (see Sec. IV A). The second terms on the right-hand side of Eqs. (7) and (8) are source terms defined by Eqs. (1) and (6):

$$\left(\frac{\partial\zeta_{\uparrow}}{\partial t}\right)_{\mathrm{S}}=\frac{N_{\downarrow}}{N_{\uparrow}}\frac{\partial\zeta_{\downarrow}}{\partial t}-\frac{1}{\mu_{\mathrm{B}}N_{\uparrow}}\frac{\partial M}{\partial t}, \tag{9}$$

$$\left(\frac{\partial\zeta_{\downarrow}}{\partial t}\right)_{\mathrm{S}}=\frac{N_{\uparrow}}{N_{\downarrow}}\frac{\partial\zeta_{\uparrow}}{\partial t}+\frac{1}{\mu_{\mathrm{B}}N_{\downarrow}}\frac{\partial M}{\partial t}. \tag{10}$$

The electric potential must satisfy the Poisson equation

$$\frac{\partial^2\varphi}{\partial z^2}=\frac{e(\delta n_{\uparrow}+\delta n_{\downarrow})}{\epsilon}, \tag{11}$$

where ϵ is the permittivity.

Internal energy density $u=u_{\uparrow}+u_{\downarrow}+u_{\mathrm{p}}$, thermal current density $q=q_{\uparrow}+q_{\downarrow}+q_{\mathrm{p}}$, and heat input per unit volume

and time $p(z,t)$ due to laser absorption satisfy the continuity equation

$$\frac{\partial u}{\partial t} + \frac{\partial q}{\partial z} = p(z,t). \tag{12}$$

Inserting Eqs. (3) and (4) and using $\partial u/\partial t = C\partial T/\partial t$, where C is the volumetric heat capacity, Eq. (12) can be separated into the three-temperature model [16],

$$C_\uparrow \frac{\partial T_\uparrow}{\partial t} - \Lambda_\uparrow \frac{\partial^2 T_\uparrow}{\partial z^2} = g_{\uparrow \mathrm{p}}(T_\mathrm{p} - T_\uparrow) + g_{\uparrow\downarrow}(T_\downarrow - T_\uparrow) + \frac{p(z,t)}{2}, \tag{13}$$

$$C_\downarrow \frac{\partial T_\downarrow}{\partial t} - \Lambda_\downarrow \frac{\partial^2 T_\downarrow}{\partial z^2} = g_{\downarrow \mathrm{p}}(T_\mathrm{p} - T_\downarrow) + g_{\uparrow\downarrow}(T_\uparrow - T_\downarrow) + \frac{p(z,t)}{2}, \tag{14}$$

$$C_\mathrm{p} \frac{\partial T_\mathrm{p}}{\partial t} - \Lambda_\mathrm{p} \frac{\partial^2 T_\mathrm{p}}{\partial z^2} = g_{\uparrow \mathrm{p}}(T_\uparrow - T_\mathrm{p}) + g_{\downarrow \mathrm{p}}(T_\downarrow - T_\mathrm{p}), \tag{15}$$

where we assumed that the laser energy is equally absorbed by majority and minority spins. The three-temperature model assumes that electrons are in a Fermi-Dirac distribution. During laser excitation, electrons are initially in a nonthermal distribution that is not captured by the three-temperature model. However, if the duration of the laser pulse is longer than the thermalization time of the electron distribution, the three-temperature model is a reasonable approximation. Further note that in the presence of a heat current, majority and minority spins are in nonthermal distributions at normal-metal/FM interfaces (compare Sec. III A). According to Ref. [14], majority and minority spins can still be described by Fermi-Dirac distributions after definition of effective temperature parameters. Hence, near the NM/FM interface, $T_\uparrow$ and $T_\downarrow$ should not be considered as real temperatures.

The three coupled heat-diffusion equations (13)–(15) can be solved independently from the charge transport equations (7) and (8) because we neglected the Peltier term in Eq. (3).

E. Boundary conditions

The multilayered structures of Experiments I and II described in Sec. II imposes the following boundary conditions to the model in the limes $\delta z \to 0$ (for the bulk properties Λ, and σ, the subscript 0, 1, 2, 3, or 4 indicates that the bulk property refers to the layer in the negative z direction from the respective interface 0, 1, 2, 3, or 4 as labeled in Fig. 1).

Boundary conditions for the transport of heat: semi-infinite dielectric substrate, continuity of the flux of heat and temperature through the sample, consideration of finite-temperature steps by thermal interface conductances G, dielectric capping, and adiabatic surface:

$$\begin{aligned}
T_\mathrm{p}(z \to -\infty) &= T_\mathrm{ambient};\\
-\Lambda_{\mathrm{p},0}\left(\frac{\partial T_\mathrm{p}}{\partial z}\right)_{z_0-\delta z} &= G_0[T_\mathrm{p}(z_0-\delta z) - T_\mathrm{p}(z_0+\delta z)];\\
-\Lambda_{s,0}\left(\frac{\partial T_s}{\partial z}\right)_{z_0+\delta z} &= 0;\\
-\Lambda_{\mathrm{p},1}\left(\frac{\partial T_\mathrm{p}}{\partial z}\right)_{z_1-\delta z} &= -\Lambda_{\mathrm{p},2}\left(\frac{\partial T_\mathrm{p}}{\partial z}\right)_{z_1+\delta z};\\
T_\mathrm{p}(z_1-\delta z) &= T_\mathrm{p}(z_1+\delta z);\\
-\Lambda_{s,1}\left(\frac{\partial T_s}{\partial z}\right)_{z_1-\delta z} &= -\Lambda_{s,2}\left(\frac{\partial T_s}{\partial z}\right)_{z_1+\delta z};\\
T_s(z_1-\delta z) &= T_s(z_1+\delta z);\\
-\Lambda_{\mathrm{p},2}\left(\frac{\partial T_\mathrm{p}}{\partial z}\right)_{z_2-\delta z} &= -\Lambda_{\mathrm{p},3}\left(\frac{\partial T_\mathrm{p}}{\partial z}\right)_{z_2+\delta z};\\
T_\mathrm{p}(z_2-\delta z) &= T_\mathrm{p}(z_2+\delta z);\\
-\Lambda_{s,2}\left(\frac{\partial T_s}{\partial z}\right)_{z_2-\delta z} &= -\Lambda_{s,3}\left(\frac{\partial T_s}{\partial z}\right)_{z_2+\delta z};\\
T_s(z_2-\delta z) &= T_s(z_2+\delta z);\\
-\Lambda_{\mathrm{p},3}\left(\frac{\partial T_\mathrm{p}}{\partial z}\right)_{z_3-\delta z} &= G_3[T_\mathrm{p}(z_3-\delta z) - T_\mathrm{p}(z_3+\delta z)];\\
-\Lambda_{s,3}\left(\frac{\partial T_\mathrm{s}}{\partial z}\right)_{z_3-\delta z} &= 0;\\
-\Lambda_{\mathrm{p},4}\left(\frac{\partial T_\mathrm{p}}{\partial z}\right)_{z_4-\delta z} &= 0;
\end{aligned} \tag{16}$$

where $s =\uparrow$ for majority spins and $s =\downarrow$ for minority spins. For Experiment I, we neglect layer FM2 in the thermal model since the total metal stack is much thicker than layer FM2.

Boundary conditions for the transport of charge: dielectric substrate, continuity of the charge current density and chemical potential through the metal stack, consideration of finite chemical potential steps by electrical interface conductances Σ, and dielectric capping:

$$\begin{aligned}
\frac{\sigma_{s,1}}{e}\left(\frac{\partial \Phi_s}{\partial z}\right)_{(z_0+\delta z)} &= 0;\\
\frac{\sigma_{s,1}}{e}\left(\frac{\partial \Phi_s}{\partial z}\right)_{(z_1-\delta z)} - S_{s,1}\sigma_{s,1}\left(\frac{\partial T_s}{\partial z}\right)_{(z_1-\delta z)} &= -\frac{\Sigma_{s,1}}{e}[\Phi_s(z_1-\delta z) - \Phi_s(z_1+\delta z)] + S_{s,1}\Sigma_{s,1}[T_s(z_1-\delta z) - T_s(z_1+\delta z)];\\
\frac{\sigma_{s,2}}{e}\left(\frac{\partial \Phi_s}{\partial z}\right)_{(z_2-\delta z)} - S_{s,2}\sigma_{s,2}\left(\frac{\partial T_s}{\partial z}\right)_{(z_2-\delta z)} &= -\frac{\Sigma_{s,2}}{e}[\Phi_s(z_2-\delta z) - \Phi_s(z_2+\delta z)] + S_{s,2}\Sigma_{s,2}[T_s(z_2-\delta z) - T_s(z_2+\delta z)].
\end{aligned} \tag{17}$$

For the multilayer of Experiment I, we assume that FM2 is a perfect spin sink,

$$\zeta_\uparrow(z_3) - \zeta_\downarrow(z_3) = 0;$$
$$\frac{\sigma_{\uparrow,3}}{e}\left(\frac{\partial\Phi_\uparrow}{\partial z}\right)_{(z_3-\delta z)} + \frac{\sigma_{\downarrow,3}}{e}\left(\frac{\partial\Phi_\downarrow}{\partial z}\right)_{(z_3-\delta z)} = 0; \quad (18)$$

while for Experiment II,

$$\frac{\sigma_{s,3}}{e}\left(\frac{\partial\Phi_s}{\partial z}\right)_{(z_3-\delta z)} = 0.$$

To describe the pulsed-laser heating, we approximate the temporal heating profile with a Gaussian function using a FWHM of 0.85 ps, which corresponds to the FWHM of correlated pump and probe pulses. Then, the heat input per unit volume and time, $p(z,t)$, in the heat-diffusion equations (13)–(15) is

$$p(z,t) = F_\mathrm{a}\frac{p_\mathrm{a}(z)}{\int_0^{z_2} p_\mathrm{a}(z)dz}\exp\left(-\frac{t^2}{2\tilde{\sigma}^2}\right), \quad (19)$$
$$z \in \{0,z_2\}, \quad t \in \{-10,10\}\ \mathrm{ps}, \quad (20)$$

where $F_\mathrm{a} = 3.7\ \mathrm{J\ m^2}$ is the absorbed fluence, $p_\mathrm{a}(z)$ is the absorption profile through the Pt/FM1 bilayer (see Sec. B), $\tilde{\sigma} = \mathrm{FWHM}/(2\sqrt{2\ln 2})$, and $z = 0$ and $z = z_2$ are the coordinates of the sapphire/Pt and FM1/Cu interfaces, respectively (compare Fig. 1).

IV. APPROXIMATIONS

The transport equations derived in Sec. III include 17 material parameters that are required for each layer of the sample. In the following, we introduce three approximations that hold for zero charge current, zero SHA, and small divergence of electronic heat current in FM1. Application of these approximations allows for a reduction of the number of free parameters and results in the simplified spin-diffusion model used by Choi *et al.* [10]. As discussed in Sec. III A, heat transport through NM/FM interfaces can create SHA, i.e., Approximation II below is not generally valid. The influence of SHA on spin diffusion is discussed in Sec. V.

A. Approximation I: Zero charge current

Under open circuit conditions, the initial charge current after application of a temperature difference relaxes on a time scale given by the dielectric relaxation time $\tau_\mathrm{dr} = \epsilon/\sigma$, where ϵ is the permittivity and σ is the electrical conductivity. In metals, τ_dr is of the order of 1×10^{-18} s. Since the temperature gradients in the experiments considered here vary on much longer time scales in comparison to electric fields, we can assume that the charge current is zero,

$$j = j_\uparrow + j_\downarrow = 0. \quad (21)$$

Inserting Eq. (2) in Eq. (21), we can substitute $\partial\varphi/\partial z$ in the charge transport equations (7) and (8). The resulting spin current, $j_\uparrow - j_\downarrow$, and the corresponding time-dependent spin-diffusion equation read

$$j_\uparrow - j_\downarrow = \frac{2\sigma_\uparrow\sigma_\downarrow}{e(\sigma_\uparrow+\sigma_\downarrow)}\left[\frac{\partial(\zeta_\uparrow-\zeta_\downarrow)}{\partial z} - eS_\uparrow\frac{\partial T_\uparrow}{\partial z} + eS_\downarrow\frac{\partial T_\downarrow}{\partial z}\right], \quad (22)$$

$$\frac{\partial(\zeta_\uparrow-\zeta_\downarrow)}{\partial t} - D\left[\frac{\partial^2(\zeta_\uparrow-\zeta_\downarrow)}{\partial z^2} - eS_\uparrow\frac{\partial^2 T_\uparrow}{\partial z^2} + eS_\downarrow\frac{\partial^2 T_\downarrow}{\partial z^2}\right]$$
$$= -\frac{\zeta_\uparrow-\zeta_\downarrow}{\tau_\mathrm{S}} + \left[\frac{\partial(\zeta_\uparrow-\zeta_\downarrow)}{\partial t}\right]_\mathrm{S}, \quad (23)$$

where $D = (\sigma_\downarrow D_\uparrow + \sigma_\uparrow D_\downarrow)/(\sigma_\uparrow+\sigma_\downarrow)$ is the spin-averaged diffusion constant and $\tau_\mathrm{S} = eN_\uparrow N_\downarrow/[\alpha(N_\uparrow+N_\downarrow)] = l_\mathrm{S}^2/D$ is the spin-relaxation time, with l_S being the spin-diffusion length. Using the equality $\partial\zeta_\uparrow/\partial t = -\partial\zeta_\downarrow/\partial t$ valid for Approximation I, the source terms due to ultrafast demagnetization become

$$\left[\frac{\partial(\zeta_\uparrow-\zeta_\downarrow)}{\partial t}\right]_\mathrm{S} = -\frac{N_\uparrow+N_\downarrow}{2\mu_\mathrm{B}N_\uparrow N_\downarrow}\frac{\partial M}{\partial t}. \quad (24)$$

Approximation I removes the material parameter ϵ from the model. However, due to spin-dependent transport in FM1, the charge accumulation at interfaces created by the initial charge current is accompanied by spin accumulation. To demonstrate that spin accumulation due to the Seebeck effect is much smaller in comparison to spin accumulation due to SDSE, it is sufficient to consider a semi-infinite homogeneous conductor with a temperature gradient $\partial T/\partial z$ perpendicular to its surface. The surface charge density is given by the electric field $E = -S\partial T/\partial z$,

$$\Sigma_\mathrm{q} = \epsilon E = -\epsilon S\frac{\partial T}{\partial z}. \quad (25)$$

Assuming a spin-asymmetry coefficient of $\beta = (\sigma_\uparrow - \sigma_\downarrow)/(\sigma_\uparrow+\sigma_\downarrow) = 0.5$, the number of spins per unit area due to the Seebeck effect is given by

$$\eta_\mathrm{SE} = \frac{\Sigma_\mathrm{q}\beta}{e} = -\frac{\epsilon}{2e}S\frac{\partial T}{\partial z}. \quad (26)$$

The steady-state solution of Eqs. (31) and (35) below for a semi-infinite conductor extended in the z direction is given by

$$\zeta_\uparrow - \zeta_\downarrow = -eS_\mathrm{S}l_\mathrm{S}\frac{\partial T}{\partial z}\exp\left(-\frac{z}{l_\mathrm{S}}\right), \quad (27)$$

where $l_\mathrm{S} = \sqrt{D\tau_\mathrm{S}}$ is the spin-diffusion length. Integration of Eq. (27) and multiplication of the result with the density of states at the Fermi energy gives the number of spins per unit area due to the SDSE,

$$\eta_\mathrm{SDSE} = -\frac{1}{2e}S_\mathrm{S}\frac{\partial T}{\partial z}\sigma\tau_\mathrm{S}. \quad (28)$$

Finally, comparing Eqs. (26) and (28), we obtain

$$\frac{\eta_\mathrm{SE}}{\eta_\mathrm{SDSE}} = \frac{\tau_\mathrm{dr}}{\tau_\mathrm{S}}\frac{S}{S_\mathrm{S}}. \quad (29)$$

The ratio of Seebeck coefficient and spin Seebeck coefficient S/S_S is of the order of 1, whereas $\tau_\mathrm{dr}/\tau_\mathrm{S} \ll 1$. Therefore, the spin accumulation is predominantly caused by the SDSE, i.e., spin accumulation due to charge accumulation is negligibly small.

B. Approximation II: Zero spin heat accumulation

Prior models for describing the SDSE assume equality of the temperatures of majority and minority spins,

$$T_\uparrow - T_\downarrow = 0. \tag{30}$$

Under this assumption, the spin current and time-dependent spin-diffusion equation become

$$j_\uparrow - j_\downarrow = \frac{2\sigma_\uparrow\sigma_\downarrow}{e(\sigma_\uparrow+\sigma_\downarrow)}\left[\frac{\partial(\zeta_\uparrow-\zeta_\downarrow)}{\partial z} - eS_S\frac{\partial T_e}{\partial z}\right], \tag{31}$$

$$\frac{\partial(\zeta_\uparrow-\zeta_\downarrow)}{\partial t} - D\left[\frac{\partial^2(\zeta_\uparrow-\zeta_\downarrow)}{\partial z^2} - eS_S\frac{\partial^2 T_e}{\partial z^2}\right] = -\frac{\zeta_\uparrow-\zeta_\downarrow}{\tau_S} - \frac{N_\uparrow+N_\downarrow}{2\mu_B N_\uparrow N_\downarrow}\frac{\partial M}{\partial t}, \tag{32}$$

where $S_S = S_\uparrow - S_\downarrow$ is the spin Seebeck coefficient, which should not be confused with the so-called spin Seebeck effect. In contrast to the SDSE, the spin Seebeck effect describes thermal generation of a spin current across the interface between a magnetic material and a normal metal based on electron-magnon interactions across that interface (compare Sec. VI C) [23]. The second term in Eq. (31) defines the spin generation rate at the FM1/Cu interface used by Choi *et al.* (compare Eq. (2) in Ref. [10]). Note that Choi *et al.* use a slightly different definition for S_S. Though this definition includes a spin-asymmetry coefficient of the electrical conductivity, Choi *et al.* assume $\sigma_\uparrow = \sigma_\downarrow$, which gives a spin Seebeck coefficient that is a factor of 2 smaller than the definition $S_S = S_\uparrow - S_\downarrow$ used here.

The three-temperature model reduces to the two-temperature model,

$$C_e\frac{\partial T_e}{\partial t} - \Lambda_e\frac{\partial^2 T_e}{\partial z^2} = g_{ep}(T_p - T_e) + p(z,t), \tag{33}$$

$$C_p\frac{\partial T_p}{\partial t} - \Lambda_p\frac{\partial^2 T_p}{\partial z^2} = g_{ep}(T_e - T_p), \tag{34}$$

where subscript e refers to electrons. Approximation II removes the parameter $g_{\uparrow\downarrow}$ and the spin dependence of C_e, Λ_e, and g_{ep} from the model.

C. Approximation III: Small divergence of electronic heat current in FM1

The remaining material parameters represent a minimum parameter set for describing spin diffusion in metals subsequent to pulsed-laser heating. However, if the characteristic time of heat diffusion through FM1 is much shorter than the rise time of the electron temperature, the Seebeck spin-diffusion term in Eq. (32) that is proportional to the divergence of the electronic heat current becomes small compared to the normal diffusion term. In that case, Eq. (32) reduces to

$$\frac{\partial(\zeta_\uparrow-\zeta_\downarrow)}{\partial t} - D\frac{\partial^2(\zeta_\uparrow-\zeta_\downarrow)}{\partial z^2} = -\frac{\zeta_\uparrow-\zeta_\downarrow}{\tau_S} - \frac{N_\uparrow+N_\downarrow}{2\mu_B N_\uparrow N_\downarrow}\frac{\partial M}{\partial t}, \tag{35}$$

which does *not* include the spin Seebeck coefficient or electron temperature. The SDSE is included in the boundary conditions, e.g., the continuity of the spin current at the interfaces [compare Eq. (17)].

The characteristic length $l_{ep} = \sqrt{\tau_{ep}D}$ over which electrons and phonons can have different temperatures is determined by electron-phonon thermalization time $\tau_{ep} = C_e/g_{ep}$ and diffusion constant $D = \Lambda_e/C_e$ of electrons [29]. For [Co/Pt] and [Co/Ni], l_{ep} is of the order of 10 nm, which is significantly larger than the thickness of FM1 of $h_{FM1} \approx 3$ nm. Therefore, the characteristic time of heat diffusion through FM1 is determined by the diffusion constant of electrons in FM1, which gives a very short time of $\tau_{FM1} = h_{FM1}^2/(4D) \approx 30$ fs. Since $T_e(t)$ varies on a much longer time scale, $[T_e(t+\tau_{FM1}) - T_e(t)]/T_e(t) \ll 1$, the spatial temperature profile is approximately linear in FM1 at each relevant time step (compare $T_\uparrow(z)$ and $T_\downarrow(z)$ in Fig. 2).

Note that Approximation III does not hold in the adjacent Pt and Cu layers, which are much thicker than FM1. However, since the spin-dependent Seebeck coefficient is zero in the nonmagnetic layers, the spin-diffusion equation still reduces to Eq. (35). Further, Approximation III does not hold for sample geometries in which most of the pump light is absorbed in a thicker ($>\sim$10 nm) ferromagnetic layer.

Approximations I–III constitute the basis of the spin-diffusion model used by Choi *et al.* [10]. In Sec. V, we question Approximation II and investigate the influence of SHA in Experiments I and II reported in Ref. [10].

V. INFLUENCE OF SHA ON SPIN DIFFUSION

Approximation II fails if the spin heat relaxation time is comparable to the spin-relaxation time. Thermalization between electrons is achieved through inelastic-scattering mechanisms, which can differ between noble metals and transition metals.

In Au, complete thermalization of electrons is achieved after approximately 1 ps [19]. Assuming a similar thermalization time in Cu, the spin heat relaxation length of Cu can be estimated as $l_{S,th}^{Cu} = \sqrt{D\tau_{S,th}^{Cu}} < 100$ nm. The electron diffusion length during thermalization of electrons with phonons is $l_{ep} = \sqrt{\frac{\Lambda_e}{g_{ep}}} \approx 60$ nm. Therefore, we conclude that thermalization of electrons in Cu at room temperature is dominated by electron-phonon scattering with spin heat diffusion length $l_{S,th}^{Cu} \approx 60$ nm.

In transition metals, collisions of electrons from different bands with different effective masses and velocities significantly contributes to the electrical and thermal resistivities. Since the coupling parameter $g_{\uparrow\downarrow}$ of Pt is unknown, we estimate an upper bound of the spin heat diffusion length of Pt of $l_{S,th}^{Pt} = \sqrt{\frac{\Lambda}{g_{ep}+4g_{\uparrow\downarrow}}} < \sqrt{\frac{\Lambda}{g_{ep}}} \approx 10$ nm [16]. Note that in the presence of spin heat accumulation in a normal metal, both majority- and minority-spin electrons are in nonthermal distributions (compare Sec. III A).

In ferromagnetic transition metals, a spin-polarized band structure results in different scattering rates for majority- and minority-spin electrons, which gives rise to a spin-dependent thermalization time. In Sec. A 3, we determine a very short spin-relaxation time of approximately 20 fs for the [Co/Pt] layer, which is significantly shorter than the

electron-phonon thermalization time of ∼0.8 ps. Experimental results reported in Ref. [30] indicate strong spin-flip scatterings at the interfaces of [Co/Pt] multilayers, which supports the short spin-relaxation times we determined. Note that for strong electron-electron coupling between minority spins, it is possible that minority spins are in a Fermi-Dirac distribution in the presence of spin heat accumulation if spin heat relaxation is dominated by spin-flip scattering.

If spin heat relaxation in [Co/Pt] is dominated by spin-flip scattering, then the spin heat diffusion length can be estimated as $l_{\mathrm{S,th}}^{[\mathrm{Co/Pt}]} \approx \sqrt{D\tau_{\mathrm{S}}} \approx 1.4$ nm. In that case, $l_{\mathrm{S,th}}$ equals the spin-diffusion length, in which both are of the order of the thickness of the [Co/Pt] layer.

Based on these estimations, it is reasonable to assume that SHA can be significant in the metal stacks considered here. In addition to these theoretical aspects, the concept of spin heat accumulation is corroborated by recent experiments that measure cross-plane giant magnetothermal resistance (CPP-GMTR) [15,16].

In the absence of SHA, the SDSE is determined by the difference $S_\uparrow - S_\downarrow = S_{\mathrm{S}}$ [compare Eq. (32)]. The presence of SHA results in different gradients $\partial T_\uparrow/\partial z$ and $\partial T_\downarrow/\partial z$. As a consequence, the SDSE depends on $S_\uparrow$ and $S_\downarrow$, or on $S_\uparrow - S_\downarrow = S_{\mathrm{S}}$ and $S_\uparrow + S_\downarrow = S$, respectively [compare Eq. (22)].

To demonstrate a possible influence of SHA on the SDSE, we analyze the measurement data reported in Ref. [10] for the [Co/Pt] sample using Eqs. (13)–(15), (22), and (23). In contrast to the simplified heat- and spin-diffusion model used by Choi *et al.*, consideration of SHA requires knowledge of the normal Seebeck coefficient S, the coupling parameter $g_{\uparrow\downarrow}$, and the spin asymmetries of electrical conductivity, thermal conductivity, and electron-phonon coupling parameter. Since S of [Co/Pt] is unknown, we use S of Co ($S_{\mathrm{Co}} = -22\ \mu\mathrm{V\ K^{-1}}$) [18]. Nguyen *et al.* measured a spin-scattering asymmetry of Co/Pt interfaces of $\beta = (\sigma_\uparrow - \sigma_\downarrow)/(\sigma_\uparrow + \sigma_\downarrow) = 0.5$ [30]. Based on the Wiedemann-Franz law, we assume that $\beta = 0.5$ also describes the asymmetry of the thermal conductivity of the Co/Pt multilayer [31]. We estimate the coupling parameter $g_{\uparrow\downarrow}$ of [Co/Pt] using the spin-relaxation time determined from the simplified heat- and spin-diffusion model (see Appendix A), which gives

$$g_{\uparrow\downarrow} \approx \frac{C_{\mathrm{e}}}{4\tau_{\mathrm{S}}} \approx 2.7 \times 10^{18}\ \mathrm{J\,m^{-3}\,K^{-1}}. \tag{36}$$

Below, we find that consideration of SHA does not significantly change the fit result for τ_{S} of [Co/Pt].

We do not consider spin-dependent electron-phonon coupling [32], which can modify SHA at time scales shorter than the electron-phonon thermalization time.

Calculated profiles of $T_\uparrow$, $T_\downarrow$, and T_{p} through the metal stack are shown in Fig. 2. During laser excitation, [Co/Pt] and Cu electrons are heated predominantly via electronic heat transport ($t = 0.4$ ps, left panel in Fig. 2). Note that due to the comparatively long duration of the pump pulses considered here (FWHM ≈0.8 ps), we assume that ballistic and superdiffusive heat transport do not significantly modify the temperatures of [Co/Pt] and Cu electrons (compare Sec. VI B). The asymmetry in the heat currents of majority and minority spins in the [Co/Pt] layer results in a splitting of $T_\uparrow$ and $T_\downarrow$. The SHA scales with the temperature rise (Fig. 2 middle panel: $t = 2$ ps; right panel: $t = 20$ ps) and persists as long as heat flows through the NM/FM interfaces.

The calculated transients of $\partial T_\uparrow/\partial z$ and $\partial T_\downarrow/\partial z$ in FM1 are shown in Fig. 3(a) for $\beta_{[\mathrm{Co/Pt}]} = 0.5$ (red and blue lines) and $\beta_{[\mathrm{Co/Pt}]} = 0$ (black line). Figure 3(b) shows data from Experiment I taken from Ref. [10] for the [Co/Pt] sample, together with the fit curve (solid line) we obtained from the spin-diffusion model under consideration of SHA, using τ_s and S_s as free parameters (for details on analysis and model parameters, see Appendices A and D).

We obtain the fit results $\tau_{\mathrm{S}} = 19$ fs and $S_{\mathrm{S}} = 12.5\ \mu\mathrm{V\ K^{-1}}$ for [Co/Pt]. Compared to the fit results that we obtain when neglecting SHA (see Appendix A 3), the fit value for S_{S} is decreased by ∼34%. This means that the presence of SHA can significantly enhance the SDSE.

We use the results obtained from Experiment I to calculate the spin accumulation in the Cu layer expected in Experiment II [Fig. 3(c)]. Comparison of the model curve with the measurement data then gives a conversion factor that relates Kerr rotation with spin accumulation in Cu. The peak of the spin accumulation is dominated by τ_{S} of the [Co/Pt] layer. Since the fit result for τ_{S} decreases by ∼5% when considering SHA, the conversion factor $\theta_{\mathrm{K}}/M_z = 8.5$ nrad A^{-1} m is ∼5% larger than the conversion factor determined without consideration of SHA (see Appendix A 4).

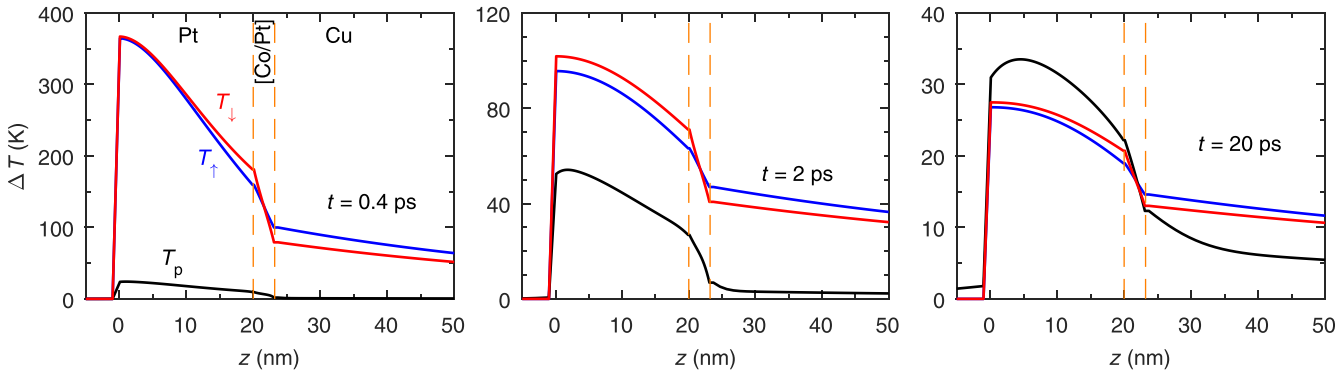

FIG. 2. Temperature profiles of majority spins, $T_\uparrow$, minority spins, $T_\downarrow$, and phonons, T_{p}, at different times steps after peak laser excitation (left panel: 0.4 ps; middle panel: 2 ps; right panel: 20 ps), calculated assuming a spin-asymmetry coefficient of the thermal conductivity of $\beta_\Lambda = (\Lambda_\uparrow - \Lambda_\downarrow)/(\Lambda_\uparrow + \Lambda_\downarrow) = 0.5$.

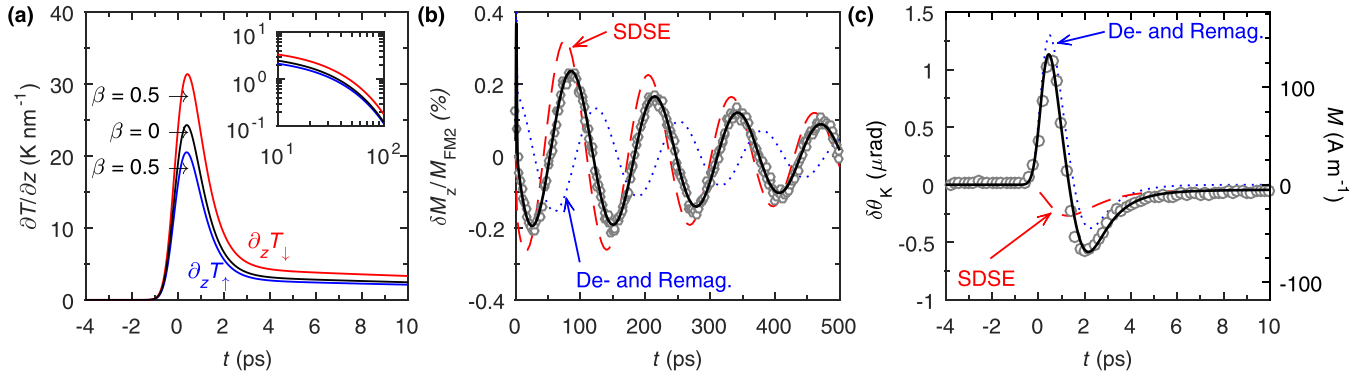

FIG. 3. (a) Gradients $\partial T_\uparrow/\partial z$ of majority spins (blue) and $\partial T_\downarrow/\partial z$ of minority spins (red) in FM1 for spin asymmetry of electronic thermal conductivity of $\beta = 0.5$. The black line shows $\partial T_e/\partial z$ for $\beta = 0$. (b) Precession data of FM2 measured with TRMOKE for [Co/Pt] as FM1. (c) Kerr rotation $\delta\theta_K$ and corresponding nonequilibrium magnetization M in Cu for [Co/Pt] as FM1. Data in (b) and (c) are taken from Ref. [10]; data in (c) is corrected by factor 1.7 (see Appendix A 4). Fit curves (solid lines) are determined using the heat- and spin-diffusion model [Eqs. (13)–(15), (22), (23)] considering spin heat accumulation. Dashed and dotted lines indicate contributions from SDSE and from de- and remagnetization, respectively.

Note that the presence of SHA can induce a SDSE in the normal-metal layers Pt and Cu, which contributes to the spin signals in Experiments I and II. Consideration of $S_{Cu} \approx 1.5\ \mu V\ K^{-1}$ and $S_{Pt} \approx -5\ \mu V\ K^{-1}$ further decreases the fit result for S_S by ∼10%.

VI. DISCUSSION

A. Can spin heat accumulation be useful?

From a material science perspective, it is interesting to point out material properties required for increasing the magnitude and time scale of thermally induced spin currents. However, optimization of the SDSE-driven spin current is complicated by the interplay of spin-dependent electrical conductivities, temperature gradients, and Seebeck coefficients. Therefore, it is useful to express the SDSE-driven spin current in Eq. (22),

$$j_\uparrow - j_\downarrow = \frac{2\sigma_\uparrow\sigma_\downarrow}{(\sigma_\uparrow+\sigma_\downarrow)}\left(-S_\uparrow\frac{\partial T_\uparrow}{\partial z} + S_\downarrow\frac{\partial T_\downarrow}{\partial z}\right), \tag{37}$$

in terms of spin-asymmetry coefficients $\beta_\Lambda \approx \beta_\sigma = (\sigma_\uparrow - \sigma_\downarrow)/(\sigma_\uparrow+\sigma_\downarrow)$, $\beta_q = (q_\uparrow - q_\downarrow)/(q_\uparrow+q_\downarrow)$, and $\beta_S = (S_\uparrow - S_\downarrow)/(S_\uparrow+S_\downarrow)$. By substituting $\sigma_\uparrow$ and $\sigma_\downarrow$ using the Wiedemann-Franz law $\sigma_\uparrow/\Lambda_\uparrow = \sigma_\downarrow/\Lambda_\downarrow \approx L_0 T_e$, where $L_0 = 2.45\times10^{-8}\ V^2\ K^{-2}$ is the Sommerfeld value of the Lorenz number, together with the Fourier law [first term in Eq. (3)], Eq. (37) becomes

$$j_\uparrow - j_\downarrow = \frac{2(\Lambda_\uparrow S_\downarrow q_\downarrow - \Lambda_\downarrow S_\uparrow q_\uparrow)}{(\Lambda_\uparrow+\Lambda_\downarrow)L_0 T_e}. \tag{38}$$

Using the spin-asymmetry coefficients β_Λ, β_q, and β_S, we finally obtain

$$j_\uparrow - j_\downarrow = \frac{Sq_e}{2L_0T_e}[(\beta_\Lambda\beta_S - 1)\beta_q + (\beta_\Lambda - \beta_S)]. \tag{39}$$

While β_Λ and β_q are limited to the interval $[-1;1]$, the magnitude of β_S can be larger than 1, since $S_\uparrow$ and $S_\downarrow$ can have opposite signs. Note that β_q is a function of β_Λ, as illustrated in Fig. 4(a).

For $\beta_S = 0$, we obtain a SHA-driven SDSE with a spin current proportional to the sum of β_q and β_Λ: $j_\uparrow - j_\downarrow = (\beta_q + \beta_\Lambda)Sq_e/(2L_0T_e)$.

For $\beta_\Lambda = \beta_q = 1$, the spin current in Eq. (39) vanishes. This is because spin diffusion in only one conduction channel is accompanied by charge diffusion. Under open circuit conditions, relaxation of charge currents occurs on much shorter time scales in comparison to the variation of the temperature gradients in our experiments (compare Sec. IV A above). This reasoning predicts that the SDSE does not occur in Heusler compounds with 100% spin polarization.

Equation (39) predicts a large SDSE in materials with large β_S and β_Λ of opposite sign. To illustrate the dependence of the SDSE on β_Λ and β_S, we consider the integral

$$I = \int (j_\uparrow - j_\downarrow)dt \tag{40}$$

over the spin current across the Cu/FM2 interface in Experiment I. Figure 4(b) maps the integral I over the two-dimensional parameter space of β_S and β_Λ for the [Co/Pt] sample assuming $S_{[Co/Pt]} = -22\times10^{-6}\ V\ K^{-1}$. It can be seen that $|I|$ scales linearly with β_S and becomes large if β_S and β_Λ have opposite signs.

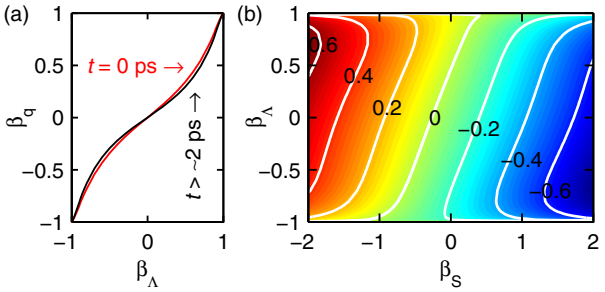

FIG. 4. (a) Spin-asymmetry coefficient $\beta_q = (q_\uparrow - q_\downarrow)/(q_\uparrow + q_\downarrow)$ of the electronic heat current as a function of $\beta_\Lambda = (\Lambda_\uparrow - \Lambda_\downarrow)/(\Lambda_\uparrow + \Lambda_\downarrow)$ at delay times as indicated. (b) Integral I of the spin current in Experiment I [compare Eq. (40)], mapped over β_Λ and β_S for the [Co/Pt] sample assuming $S_{[Co/Pt]} = -22\times10^{-6}$ V K^{-1}. White lines are contours of constant I as indicated in the graph in units of A s m^{-2}.

B. Spin transport and ultrafast demagnetization

In Sec. III B, we assume that ultrafast demagnetization of the [Co/Pt] layer creates spin accumulation in the [Co/Pt] layer [compare Eq. (1)], and propose electron-magnon scattering as a possible physical mechanism that could explain this assumption. According to this interpretation, both ultrafast demagnetization of [Co/Pt] and spin transport are caused by local scattering mechanisms in the [Co/Pt] layer that are driven by a temperature difference between electrons and the lattice. Due to the highly conductive metal-metal interfaces and the only 3-nm-thick [Co/Pt] layer, the spin accumulation created in the [Co/Pt] layer diffuses into the adjacent Cu and Pt layers. Spin relaxation to the lattice predominantly occurs in the Pt and the [Co/Pt] layers with short spin-relaxation times, and in the CoFeB layer that acts as a spin sink in Experiment I. For Experiment II, the peak nonequilibrium magnetization in the Cu layer at ∼0.5 ps is of the order of 150 A m^{-1} [compare Figs. 3(c) and 7(b)]. The peak magnetization loss in the [Co/Pt] layer at ∼0.5 ps is of the order of 10 500 A m^{-1} (compare Fig. S1(a) in the supplemental material of Ref. [10]). Hence, the maximum nonequilibrium magnetic moment in the 100-nm-thick Cu layer corresponds to approximately 50% of the maximum loss of magnetic moment of the 3-nm-thick [Co/Pt] layer. The assumption of conventional spin diffusion in the experiments of Choi *et al.* is corroborated by their measurement of a spin signal that propagates in Cu with a velocity more than one order of magnitude smaller than the group velocity of electrons [9]. However, a description based on a conventional heat- and spin-diffusion model fails at the femtosecond time scale, where electrons are in a nonthermal distribution, and at length scales smaller than the mean free path of electrons.

The superdiffusive spin transport (SDST) theory describes the transition from ballistic electron transport to electronic thermal diffusion and thus captures the nonequilibrium dynamics of electrons in nanoscale metal heterostructures subsequent to laser excitation [11]. SDST proposes a nonlocal mechanism for ultrafast demagnetization and can be interpreted as an ultrafast spin-dependent Seebeck effect that acts for a very short time of a few hundred fs [22]. According to the SDST theory, the magnetization loss measured during ultrafast demagnetization is caused by spin transport out of the probed region, e.g., into adjacent normal-metal layers. The assumption of superdiffusive spin transport initiated by direct excitation of ferromagnetic metals with femtosecond laser pulses is corroborated by the results of Melnikov *et al.*, who measure a spin signal that propagates in Au with a velocity close to the group velocity of electrons [3]. However, the experiment of Melnikov *et al.* does not exclude ultrafast demagnetization via electron-magnon scattering and local angular momentum transfer to the lattice because the contribution of superdiffusive spin transport to the total magnetization loss in the ferromagnetic layer is not quantified.

Eschenlohr *et al.* measure ultrafast demagnetization of a 15 nm Ni thin film deposited on a Al foil by indirect laser excitation through a 30-nm-Au capping layer [8]. Since the major amount of absorbed laser energy is transferred to Au electrons, Eschenlohr *et al.* assume that ultrafast demagnetization of the Ni layer is caused by superdiffusive spin transport (SDST) out of the Ni layer into the Al foil. Eschenlohr *et al.* state that based on their experimental findings, several other spin-flip mechanisms, such as electron-phonon or electron-magnon scattering, become much less likely as the main driving mechanism of ultrafast demagnetization [8]. Though they admit "in our experiment it could still be that hot nonequilibrium electrons reach the magnetic layer fast enough to rapidly heat the phonons and magnons in it," they argue against this possibility by stating "recent experiments on Ni however showed that this heating requires 1–2 ps for the phonons," and conclude "the observed demagnetization in Au/Ni however proceeds much faster (within ≈0.5 ps), which deems a purely thermally driven demagnetization unlikely for the Au/Ni system" [8].

We think that the reasoning of Eschenlohr *et al.* is not sufficient to exclude local transfer of angular momentum due to the following reasons. First, there is experimental and theoretical evidence that magnon emission by hot electrons can occur on a femtosecond time scale [33]. Second, ultrafast demagnetization via local angular momentum transfer does not require that the temperature of phonons, which dominate the total heat capacity, rises on a femtosecond time scale. Third, in contrast to the nonlocal measurements of spin signals provided by Melnikov *et al.* and by Choi *et al.*, the local measurement of ultrafast demagnetization reported by Eschenlohr *et al.* does not provide experimental evidence of spin transport.

We conclude that the physical mechanisms responsible for spin transport during ultrafast demagnetization are still unclear and can differ depending on time scale and sample architecture studied.

C. Longitudinal spin Seebeck effect

In the longitudinal spin Seebeck effect (LSSE) [34], a temperature difference imposed to a normal-metal/FM bilayer induces spin transport across the normal-metal/FM interface. Based on current LSSE theories, the spin current can be driven by two forces: a temperature difference between electrons and magnons across the normal-metal/FM interface [35], and a magnon temperature gradient in the FM layer [36]. For the driving force of magnon temperature gradient to be significant, it has been reported that the thickness of the magnetic insulator layer must be larger than the magnon diffusion length [37,38]. Since layer FM1 is only 3 nm thick, and since the highly conductive metal-metal interfaces only allow for small temperature differences across the interface, we assume that possible LSSE spin currents are negligibly small. Furthermore, LSSE measurements that are based on the inverse spin Hall effect use magnetic insulators because, for ferromagnetic conductors, the LSSE cannot be distinguished from the anomalous Nernst effect. In other words, the magnitude of the LSSE in ferromagnetic conductors is unknown.

VII. CONCLUSION

The pump-probe approach discussed and analyzed in this work provides a promising experimental platform for the generation and detection of spin-diffusion currents. We demonstrated that spin diffusion via the spin-dependent Seebeck effect is influenced by spin heat accumulation. Engineering of the thermal transport properties of majority

and minority spins separately can provide a new route for optimizing the spin-dependent Seebeck effect. Further experimental and theoretical work is required to determine a physical mechanism that explains the transient spin-diffusion currents during ultrafast de- and remagnetization. Our pump-probe approach and the heat- and spin-diffusion model presented here are also applicable for studying laser-induced Seebeck spin tunneling [39] and thermal spin transfer torques across a tunnel barrier [40] at ps time scales.

ACKNOWLEDGMENTS

This work was carried out in part at the Frederick Seitz Materials Research Laboratory Central Research Facilities, University of Illinois. Financial support by the U.S. Army Research Office under Contract No. W911NF-14-1-0016 and by the Deutsche Forschungsgemeinschaft (KI 1893/1-1) are kindly acknowledged.

APPENDIX A: REANALYSIS OF DATA FROM CHOI *et al.* USING THE SIMPLIFIED MODEL

Choi *et al.* approximate the temporal heating profile by a trapezoidal function and assume an exponentially decaying heating profile with a decay length of 20 nm [10]. Here we consider a Gaussian temporal heating profile and approximate the spatial heating profile with the optical absorption profile (compare Sec. III E). To compare our findings with those of Choi *et al.*, we reanalyze their data using the simplified heat- and spin-diffusion model described by Eqs. (31) and (33)–(35). We solve the model for $T_e(z,t)$ and $T_p(z,t)$ and $(\zeta_\uparrow - \zeta_\downarrow)(z,t)$ using a finite-difference method. As discussed below, we use a different fitting procedure compared to Choi *et al.* Furthermore, we provide a discussion of the sensitivities of the measurements to the model parameters and of the accuracy of the fit results.

1. Determination of $\partial T_e/\partial z$

Determination of T_e from the two-temperature model given by Eqs. (34) and (35) requires knowledge of the spatial and temporal heating profile of electrons in the sample. Choi *et al.* assume a spatial heating profile that decays exponentially with a decay length of 20 nm, which is larger than the optical penetration depth in Pt of ∼10 nm [10]. Choi *et al.* assume that the increased heating depth originates from the initially ballistic motion of laser-excited electrons. Here, we assume that the optical absorption profile represents a good approximation for the heating profile, since the inelastic mean free path of laser-excited electrons in Pt of ∼5 nm is well below the optical penetration depth [21]. We calculate the optical absorption profile using an transfer matrix optical model (see Appendix B). The cross correlation of pump and probe pulses measured at the sample using a GaP detector gives the temporal heating profile that is Gaussian in shape with a FWHM of $\delta \approx 0.8$ ps. Note that the sapphire substrate does not significantly affect the pulse duration. The absorbed laser fluence is $F_{abs} = 3.7$ J m^{-2}.

Choi *et al.* measured the temperature responses of the Pt and Cu layers using time-domain thermoreflectance (TDTR) [10]. The TDTR signal is dominated by the temperature of the phonons. Only during laser excitation can the high-temperature excursions of electrons as well as the nonthermal phonon distribution significantly modify the thermoreflectance signal [see deviation between black line and black squares in Fig. 5(a) for $t < 2$ ps]. At picosecond time scales, thermal transport from Pt electrons to Cu phonons depends on thermal conductivities and electron-phonon coupling parameters [29]. Therefore, the TDTR data can be used to determine g_{ep} of Pt and Cu (compare sensitivity plots in Appendix C).

Choi *et al.* determine g_{ep} of Pt from the temperature rise of Cu phonons at ∼1 ps and obtain $g_{ep,Pt} = 42 \times 10^{16}$ W m^{-3} K^{-1}. This approach can result in a large error due to the following reasons: (1) The sensitivity of T_{Cu} to g_{ep} of Pt peaks at $t \approx 3$ ps; at $t = 1$ ps, the sensitivity is small, comparable to the sensitivity of T_{Cu} to g_{ep} of Cu [compare Fig. 9(a)]. (2) The TDTR data for T_{Cu} is normalized to the model prediction at $t = 200$ ps. At this time scale, T_{Cu} is sensitive to the additional heat capacity of the capping layer, which is not considered in the thermal model used by Choi *et al.* After determination of g_{ep} of Pt, Choi *et al.* determine $g_{ep} = 7 \times 10^{16}$ W m^{-3} K^{-1} of Cu from the temperature responses of Pt and Cu between 10 and 200 ps [10].

Here, we use a slightly different approach. For Cu, we assume $g_{ep} = 7 \times 10^{16}$ W m^{-3} K^{-1} as determined in Ref. [41] on Pt/Cu bilayers using TDTR. Based on the sensitivity plots shown in Figs. 9(a) and 9(b), we determine g_{ep} of Pt from a weighted least-squares fit of the solution of the two-temperature model [Eqs. (33) and (34)] to the temperature rises of Pt and Cu phonons at delay times between 2 and 20 ps. The temperature responses measured are normalized to the two-temperature model at a delay time of 200 ps, when the temperature through the metal stack is approximately uniform. We obtain $g_{ep,Pt} = (29 \pm 4) \times 10^{16}$ W m^{-3} K^{-1}. Fit curves are shown in Fig. 5(a); model parameters are summarized and discussed in Appendix D.

The error indicates the statistical uncertainty as determined from the condition $\sigma^2 < 2\sigma_{min}^2$ for the variance between model prediction and measurement data, where σ_{min} is the variance when $g_{ep,Pt}$ assumes the fit value [compare Fig. 10(a)]. Note that the error range can be significantly larger due to systematic errors, e.g., from uncertainties in thermal conductivities and thicknesses of the metal layers. Furthermore, $g_{ep,Pt}$ should be considered as an effective electron-phonon coupling parameter that includes the influence of the initially nonthermal electron distribution with reduced electron-phonon coupling [42]. The discrepancy with $g_{ep,Pt} = 42 \times 10^{16}$ W m^{-3} K^{-1} determined by Choi *et al.* [10] originates from the different fitting procedure and from the different heating depth considered.

Also shown in Fig. 5(a) as blue triangles is TRMOKE data measured through the Pt layer, which indicates the temperature response of magnons in FM1. The discrepancy between the values obtained by Choi *et al.* and the values determined in this work originate from the different fitting procedure and from the different spatial heating depths considered (compare above). Note that g_{ep} of Pt determined here is more than a factor of three smaller than the value reported in Ref. [43] determined using optical pump-probe reflectivity measurements.

The TRMOKE data indicates a remagnetization time shorter than the thermalization time of electrons with phonons

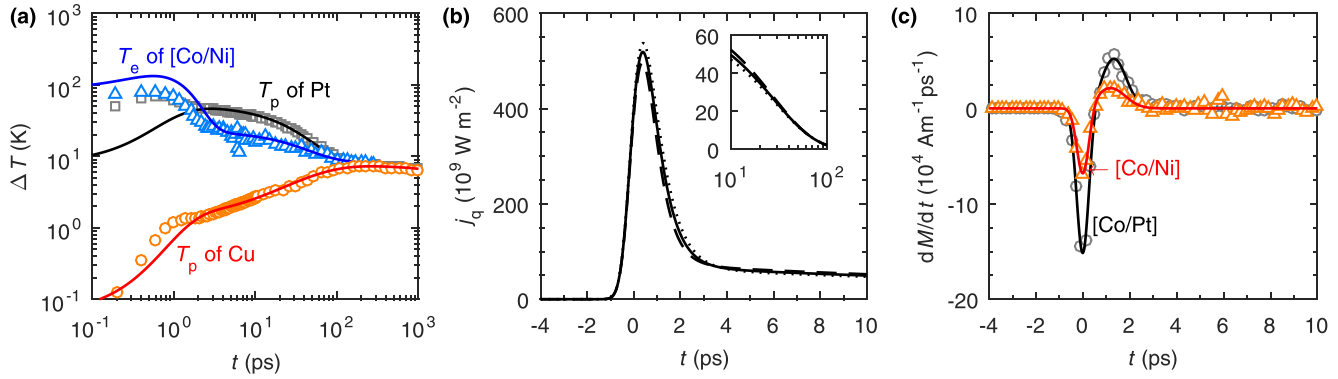

FIG. 5. (a) Temperature transients of phonons in Pt (black), phonons in Cu (red), and magnons in FM1 [Co/Ni] (blue). Squares are TDTR data measured at the Pt side, circles are TDTR data measured at the Cu side, and triangles are TRMOKE data measured through the Pt layer, taken from Ref. [10]. Solid lines are fit curves. (b) Electronic thermal current density j_q in [Co/Ni] calculated using the two-temperature model. Dashed and dotted lines indicate possible variations of j_q from an uncertainty in electron-phonon coupling parameters of Pt of $g_{ep,Pt} = (29 \pm 4) \times 10^{16}$ W m^{-3} K^{-1}. (c) Time derivative of the magnetization, $\partial M/\partial t$, of layer FM1 (triangles: [Co/Ni], circles: [Co/Pt]), taken from Ref. [10]; solid lines are fit curves using a double Gaussian function.

predicted from the two-temperature model [compare blue solid line in Fig. 5(a) that shows T_e in FM1]. This deviation could originate, e.g., from underestimated electron-phonon coupling in FM1. The TDTR data measured on the Cu side shows a hump at ∼1 ps, which indicates a significant temperature excursion of Cu electrons due to fast electronic heat transport contributing to the TDTR signal.

We use the electron-phonon coupling parameters determined to calculate the electron temperature gradient, $\partial T_e/\partial z$ in FM1. Figure 5(b) shows the calculated electronic heat current j_q in the [Co/Ni] layer. According to the time evolution of j_q, the spin current driven by $\partial T_e/\partial z$ must peak at short-time scales during laser excitation (<∼1 ps) and continues to act over longer time scales, up to ∼100 ps. The sensitivity of $\partial T_e/\partial z$ to various materials parameters is shown in Fig. 9(c). Besides electronic thermal conductivity of FM1, $\partial T_e/\partial z$ is dominated by electron-phonon coupling parameter and electronic heat capacity of Pt at short-time scales (<∼4 ps). At time scales longer than ∼4 ps, $\partial T_e/\partial z$ is dominated by electronic thermal conductivity of the FM layer and electron-phonon coupling of the Pt layer, since the latter determines the amount of laser energy stored in the Pt phonons after laser excitation. Dashed and dotted lines in Fig. 5(b) indicate variations of j_q when assuming an uncertainty of $g_{ep,Pt} = (29 \pm 4) \times 10^{16}$ W m^{-3} K^{-1}, as determined above.

2. Determination of $\partial M/\partial t$

The magnetization transient of FM1 subsequent to laser excitation can be determined empirically by comparing transient Kerr rotation with static Kerr rotation measured through the Pt layer and multiplying the results with the saturation magnetization of FM1. Numerical differentiation then gives the de- and remagnetization rates shown in Fig. 5(c). We fit the double Gaussian function

$$f(t) = y_0 + \sum_{i=1}^{2} A_i \exp\left[-\left(\frac{t - t_i}{w_i}\right)^2\right] \qquad \text{(A1)}$$

to the demagnetization rate and use the fit curve as input for the source term defined by Eq. (1). According to the time behavior of $\partial M/\partial t$, ultrafast demagnetization creates a pulselike spin current that acts at short-time scales of ∼1 ps and changes its polarity at ∼0.5 ps.

3. Modeling of Experiment I: Thermal spin-transfer torque

Experiment I probes the magnetization dynamics of layer FM2 upon laser excitation of the Pt transducer [compare Fig. 1(a)]. Magnetization precession driven by spin-transfer torque can be described by the Landau-Lifshitz-Gilbert-Slonczewski equation [44],

$$\frac{\partial \mathbf{m}}{\partial t} = -\gamma_e \mu_0 \mathbf{m} \times \mathbf{H}_{\text{eff}} + \alpha_G \mathbf{m} \times \frac{\partial \mathbf{m}}{\partial t} + \frac{\mu_B (j_\uparrow - j_\downarrow)}{e M_S h} \mathbf{m} \times (\mathbf{m} \times \mathbf{e}_z), \qquad \text{(A2)}$$

where $\mathbf{m}$ and $\mathbf{e}_z$ are unit vectors parallel to the magnetization vectors of layers FM2 and FM1, respectively; γ_e is the free electron gyromagnetic ratio, μ_0 is the permeability, H_{eff} is the effective magnetic field in FM2, α_G is the Gilbert damping constant of FM2, $j_\uparrow - j_\downarrow$ is the spin current absorbed by FM2, and M_S and h are saturation magnetization and thickness of FM2.

Layer FM2 serves as an integrating detector for spin currents. A weak spin source that is *not* detectable with Experiment II may still drive a clearly resolvable precession of FM2 in Experiment I, if the spin current acts over sufficiently long-time scales. In the measurements considered, the SDSE produces spin current for ∼100 ps. Amplitude and phase of the precession of FM2 contain information about τ_S and S_S of FM1, which we consider as a free parameter in the spin-diffusion model.

We assume that the relative change in the measured Kerr rotation is equal to the relative change in the out-of-plane component of the magnetization of FM2,

$$\frac{\delta \theta_{K,z}}{\theta_K} = \frac{\delta M_z}{M_{FM2}}, \qquad \text{(A3)}$$

where $2\theta_K$ is the change in static Kerr rotation measured when saturating the magnetization from positive to negative out-of-

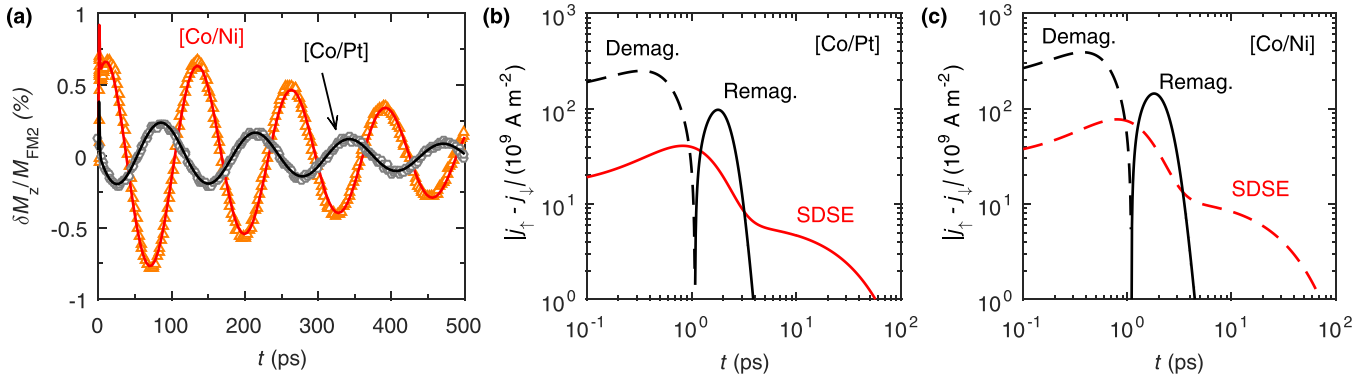

FIG. 6. (a) Precession of layer FM2 measured with TRMOKE for [Co/Ni] (triangles) and [Co/Pt] (circles) as FM1; data is taken from Ref. [10]; solid lines are fit curves using the simplified spin-diffusion model [Eqs. (31) and (35)] and the Landau-Lifshitz-Gilbert (LLG) equation [Eq. (A2)]. (b),(c) Calculated absolute spin current through the Cu/FM2 interface, driven by de- and remagnetization (black curves) and by spin-dependent Seebeck effect (red curves) for (b) [Co/Pt] and (c) [Co/Ni] as FM1. Dashed lines indicate negative spin currents.

plane directions, and M_{FM2} is the saturation magnetization of FM2.

To model Experiment I, we assume that FM2 is a perfect spin sink connected to the spin current in Cu through a spin-mixing conductance, $G_{\uparrow\downarrow}$, which represents a further unknown parameter. We assume $G_{\uparrow\downarrow} = 0.56 \times 10^{15}\ \Omega^{-1}\ \mathrm{m}^{-2}$, theoretically calculated for Co/Cu interfaces [45]. To determine the free parameters τ_S and S_S of FM1, we use a least-squares fit of the solution of the simplified spin-diffusion model [Eqs. (31) and (35)] to the TRMOKE data, reported by Choi *et al.* [10]. We obtain $\tau_S = 20^{+31\%}_{-23\%}$ fs and $S_S = 18^{+17\%}_{-5\%}\ \mu\mathrm{V\ K}^{-1}$ for [Co/Pt] and $\tau_S = 129^{+139\%}_{-69\%}$ fs and $S_S = -26^{+45\%}_{-26\%}\ \mu\mathrm{V\ K}^{-1}$ for [Co/Ni]. The errors originate from three error sources discussed below. Figure 6(a) shows the TRMOKE data together with the fit curves. Figure 6(b) and 6(c) show the calculated contributions from ultrafast demagnetization and from SDSE to the spin current that flows into FM2 as a function of time for the [Co/Pt] and [Co/Ni] samples, respectively. Model parameters are summarized in Appendix D.

There are at least three main error sources in the analysis of Experiment I: (1) the electron-phonon coupling parameter of Pt, which dominates the electronic heat current [compare Fig. 9(c)]; (2) the spin-mixing conductance of the Cu/FM2 interface, which affects the amplitude of the precession; and (3) the noise in the measurement, which affects the accuracy of the fit. To see the effect of the systematic error sources (1) and (2), we consider the uncertainty $g_{ep,Pt} = (29 \pm 5) \times 10^{16}$ W m^{-3} K^{-1} from the noise in the thermal measurement (compare Sec. A 1) and assume an uncertainty of 50% in $G_{\uparrow\downarrow}$ of the Cu/FM2 interface. To quantify the statistical error source (3), we use contours of constant variance $\sigma^2 = 2\sigma_{fit}$ between model prediction and measurement data in the two-dimensional parameter space of τ_S and S_S, where σ_{fit} is the variance when τ_S and S_S assume their fit values [see Fig. 10(b)]. The resulting error ranges are listed in Table I. For [Co/Pt], the error is dominated by the error from the noise. For [Co/Ni], the error is dominated by the errors from the spin-mixing conductance and from the noise.

Choi *et al.* analyzed Experiments I and II simultaneously and obtained, for [Co/Pt], $\tau_S = 20$ fs and $S_S = 12\ \mu\mathrm{V\ K}^{-1}$, and for [Co/Ni], $\tau_S = 100$ fs and $S_S = -24\ \mu\mathrm{V\ K}^{-1}$, which is in reasonable agreement with our results. A discussion of the short spin-relaxation times of the different signs of the spin Seebeck coefficients of [Co/Pt] and [Co/Ni] can be found in Ref. [10].

4. Modeling of Experiment II: Spin accumulation

Experiment II probes spin accumulation in the Cu layer upon laser excitation of the Pt transducer [compare Fig. 1(b)]. Since the relation between Kerr rotation and spin accumulation in Cu is unknown, the model curves have to be normalized to the measurement data to determine the free parameters τ_S and S_S of FM1. Though the fit results we obtain are close to the fit results from Experiment I, the statistical error range caused by the noise in the measurement is too large for the fit results to be meaningful.

Therefore, we use the fit results obtained from Experiment I to calculate the spin accumulation in the Cu layer expected in Experiment II. Comparison of the model curve with the measurement data then allows for determination of the conversion factor that relates Kerr rotation with spin accumulation in Cu. Figure 7(a) shows the Kerr rotation in the Cu layer measured by Choi *et al.* [10] for the [Co/Pt] and [Co/Ni] samples. Solid lines are the model curves normalized to the measurement data. Figures 7(b) and 7(c) show the calculated contributions from de- and remagnetization and from SDSE to the spin accumulation in the Cu layer for the [Co/Pt] and [Co/Ni] samples, respectively. Model parameters are summarized in Appendix D.

TABLE I. Error propagation from three error sources into the error in the spin-relaxation time, $\delta\tau_S$, and into the error in the spin Seebeck coefficient, δS_S, of [Co/Pt] and [Co/Ni]. $\delta g_{ep,Pt}$: relative error in electron-phonon coupling parameter of Pt; $\delta\Sigma_{\uparrow\downarrow}$: relative error in spin-mixing conductance of the Cu/FM2 interface; $\sigma^2 < 2\sigma^2_{min}$: condition for estimating the error from the noise in the measurement (compare Sec. A 3).

	$\delta g_{ep,Pt} = \pm 14\%$	$\delta\Sigma_{\uparrow\downarrow} = \pm 50\%$	$\sigma^2 < 2\sigma^2_{min}$
$\delta\tau_S^{[Co/Pt]}$	$^{+11\%}_{-9\%}$	$^{+21\%}_{-7\%}$	$^{+20\%}_{-20\%}$
$\delta S_S^{[Co/Pt]}$	$<^{+1\%}_{-1\%}$	$^{+12\%}_{-4\%}$	$^{+12\%}_{-3\%}$
$\delta\tau_S^{[Co/Ni]}$	$^{+22\%}_{-18\%}$	$^{+38\%}_{-12\%}$	$^{+132\%}_{-65\%}$
$\delta S_S^{[Co/Ni]}$	$^{+6\%}_{-5\%}$	$^{+13\%}_{-5\%}$	$^{+43\%}_{-25\%}$

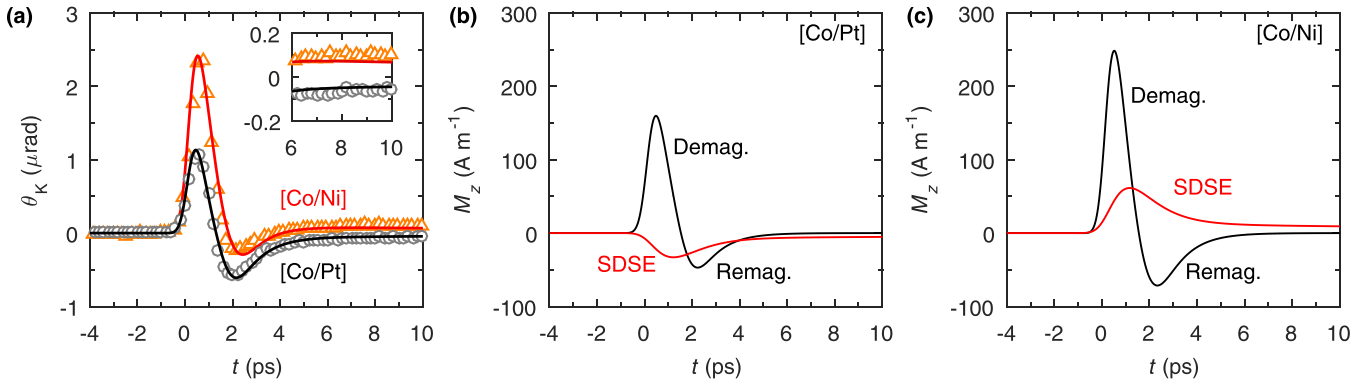

FIG. 7. (a) Kerr rotation θ_K in Cu measured for [Co/Ni] (triangles) and [Co/Pt] (circles) as FM1, taken from Ref. [10] and corrected by factor 1.7 (see main text). Solid lines are fit curves using the simplified spin-diffusion model [Eqs. (31) and (35)]. (b),(c) Calculated nonequilibrium magnetization M_z in Cu driven by de- and remagnetization (black curves) and by spin-dependent Seebeck effect (red curves) for the (a) [Co/Pt] and (b) [Co/Ni] as FM1.

To determine the conversion factor, we compare the peak height at ∼0.5 ps of the Kerr rotation measured and of the nonequilibrium magnetization predicted. We obtain the conversion factors $\theta_K/M_z = 8^{+32\%}_{-22\%}$ nrad A^{-1} m for the [Co/Pt] sample and $\theta_K/M_z = 8^{+100\%}_{-30\%}$ nrad A^{-1} m for the [Co/Ni] sample. The errors consider error propagation from τS and S_S of [Co/Pt] (compare Sec. A 3). Note that the calibration of the measurement setup used in Refs. [9,10,12] to convert the voltages measured by the rf lock-in into angles contains an error. The corrected Kerr rotations shown in Fig. 7(a) are a factor of 1.7 larger than the Kerr rotations reported in Ref. [10]. The correction affects the conversion factor that relates Kerr rotation with spin accumulation, which is a factor of approximately 1.7 larger than in Ref. [10].

APPENDIX B: ABSORPTION PROFILE

We calculate the absorption profile of laser light using a transfer matrix optical model considering optical constants of 1.76, $2.7 + i5.9$, $0.2 + i4.87$, and 1.73 for sapphire, Pt, Cu, and capping oxide layers. We assume that the optical constants of FM1 are equal to the optical constants of Pt. Figure 8 shows the normalized absorption profile $p(z)$ and the integral $P(z) = \int_0^z p(\tilde{z})d\tilde{z}$.

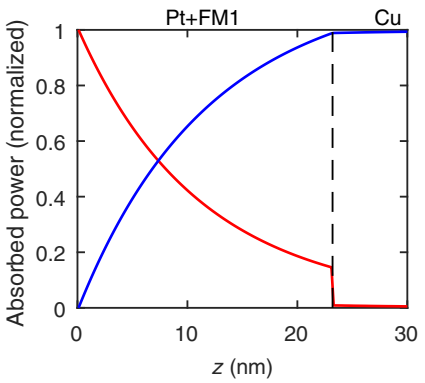

FIG. 8. Normalized differential absorption profile $p_a(z)$ (red) and absorption profile $\int_0^z p_a(\tilde{z})d\tilde{z}$ (blue) of laser light.

APPENDIX C: SENSITIVITY PLOTS AND ERROR CONTOURS

To quantify the sensitivity of variable Y with respect to parameter X, we use the sensitivity coefficient $S_X = \partial \ln Y/\partial \ln X$, which compares the relative change in Y with the relative change in X. Sensitivity coefficients for Cu temperature, Pt temperature, and electronic temperature gradient in FM1 are plotted in Figs. 9(a)–9(c), respectively. The three panels in figures (a)–(c) show the sensitivity coefficients with respect to the parameter's thermal conductivity Λ, electronic heat capacity coefficient γ, and electron-phonon coupling parameters g_{ep}, respectively, for the Cu, FM1, and Pt layers as indicated.

Figure 10(a) shows the quality of the fit as a function of the free parameter $g_{ep,Pt}$ in the thermal analysis. For the spin diffusion analysis, Fig. 10(b) shows contours of constant variance $\sigma^2 = \sigma^2_{min}$ between model prediction and measurement data in the two-dimensional parameter space of $|S_S|$ and τ_S, where σ^2_{min} is the variance when the parameters assume their fit values.

TABLE II. Model parameters [10]. h: layer thickness; σ: electrical conductivity; Λ: thermal conductivity; C: volumetric heat capacity; γ: electronic heat capacity coefficient; g_{ep}: electron-phonon coupling parameter. The choice of the model parameters not explicitly stated in Ref. [10] is discussed in Appendix D.

	MgO	Cu	[Co/Pt]	[Co/Ni]	Pt	Sapphire
h (10^{-9} m)	15	100	3.2	3.2	20	5×10^5
σ (10^8 Ω^{-1} m^{-1})	0	39	2.3	3.0	6.6	0
Λ_e (W m^{-1} K^{-1})	0	300	20	26	50	0
Λ_p (W m^{-1} K^{-1})	40	5	1	1	2	30
C (10^6 J m^{-3} K^{-1})	3.27	3.45	3.15	3.89	2.85	3.08
γ (J m^{-3} K^{-2})	0	97	699	930	721	0
g_{ep} (10^{16} W m^{-3} K^{-1})	0	7[a]	29[b]	29[b]	29[c]	0

[a]Taken from Ref. [41].
[b]Assumed to equal g_{ep} of Pt.
[c]Determined in this work (Sec. A 1).

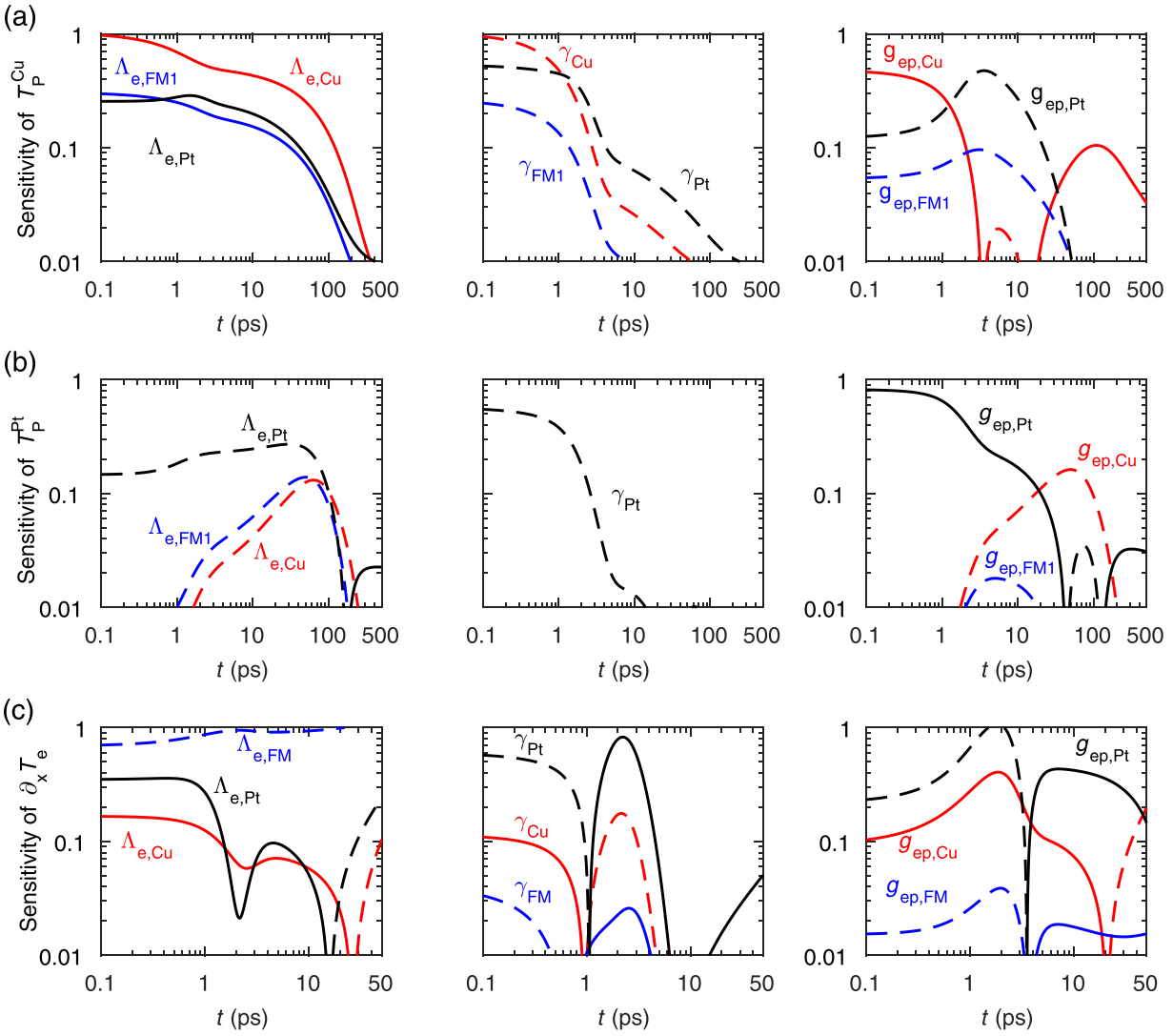

FIG. 9. Absolute value of the sensitivity coefficients for (a) temperature of Cu phonons, (b) temperature of Pt phonons, and (c) electronic temperature gradient in FM1. Dashed lines indicate negative sensitivity coefficients.

APPENDIX D: MODEL PARAMETERS AND DETAILS

Metal stacks investigated by Choi *et al.* are schematically illustrated in Fig. 1. As layer FM1, Choi *et al.* use [Co/Pt] and [Co/Ni] layers that consist of $[Co(0.2)/Pt(0.4)]_{\times 5}/Co(0.2)$ and $[Co(0.2)/Ni(0.4)_{\times 5}/Co(0.2)]$, respectively. Model parameters used by Choi *et al.* are summarized in Table II [10]. Layer FM2 is neglected in the thermal model due to its small thickness compared to the total metal stack. Electrical conductivities are determined using sheet resistivity measurements; density of states at the Fermi energy are determined by the electronic heat capacity coefficient γ, $N(E_F) = 3\gamma/(\pi^2 k_B^2)$; thermal conductivities are estimated from the sheet resistivity measurements using the Wiedemann-Franz law; total heat capacities are taken from literature values; and the electronic heat capacity is assumed to vary linearly with temperature, $C_e = \gamma T$. Choi *et al.* assume a thermal interface conductance of 100 MW m^{-2} K^{-1} for the sapphire/Pt interface [10]. We assume the same value also for the Cu/MgO interface. Since FM1 is a ∼3-nm-thin heterogeneous multilayer, we do not consider extra thermal resistances at Pt/FM1 and FM1/Cu interfaces. We approximate g_{ep} of FM1 with g_{ep} of Pt since the sensitivity of the electronic temperature gradient to g_{ep} of FM1 is negligibly small [compare Fig. 9(c)]. Apart from C_e,

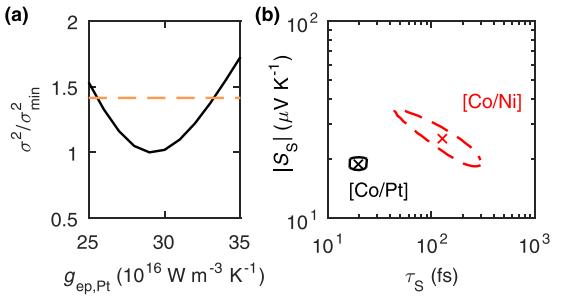

FIG. 10. (a) Quality of the fit, σ^2/σ^2_{min}, as a function of the free parameter $g_{ep,Pt}$. (b) Contours of constant variance $\sigma^2 = 2\sigma^2_{min}$ between model prediction and measurement data in the two-dimensional parameter space of $|S_S|$ and τ_S, where σ^2_{min} is the variance when the parameters assume their fit values.

we assume that the other material parameters do not change with temperature. Since the electron temperature excursion remains below 200 K during laser excitation, and is only of the order of 10 K after laser excitation, the assumption of constant material parameters (apart from C_e) is a reasonable approximation. For example, Lin *et al.* predict significant changes of g_{ep} of Pt for temperatures of the order of 1000 K and larger [46]. Thermal transport in metal is dominated by electrons. However, the phonon thermal conductivities of Pt and of Cu influence the heat transport across the sapphire/Pt and the Cu/MgO interfaces at time scales of the order of 100 ps. Since the TDTR data is normalized to the model prediction at $t = 200$ ps, errors in the phonon thermal conductivities can result in errors of the fit parameters. Here, we can only roughly estimate the phonon thermal conductivities in the metals.

Choi *et al.* assume the following electrical interface conductances: $\Sigma = 1.5 \times 10^{15}\ \Omega^{-1}\ \mathrm{m}^{-2}$ for the Pt/[Co/Pt] and the Pt/[Co/Ni] interfaces, $\Sigma = 1 \times 10^{15}\ \Omega^{-1}\ \mathrm{m}^{-2}$ for the [Co/Pt]/Cu interface, and $\Sigma = 3 \times 10^{15}\ \Omega^{-1}\ \mathrm{m}^{-2}$ for the [Co/Ni]/Cu interface [10]. The spin-mixing conductance across the Cu/FM2 interface is estimated with $G_{\uparrow\downarrow} + 0.56 \times 10^{15}\ \Omega^{-1}\ \mathrm{m}^{-2}$, as reported for Co/Cu interfaces [45].

Spin-relaxation times of Pt and Cu ($\tau_{s,Cu} = 17$ ps, $\tau_{s,Pt} = 0.5$ ps) are calculated using $\tau_S = l_S^2/D$ and assuming $l_S^{Pt} \approx 10$ nm and $l_S^{Cu} \approx 400$ nm. The parameters used for calculation of spin-transfer torque driven magnetization dynamics [Eq. (A2)] are $\gamma_e = 1.76 \times 10^{-11}$ rad s^{-1} T^{-1}, $\alpha_G = 0.05$, $M_S = 1.2 \times 10^6$ A m^{-1}, and $H_{eff} = 2.2 \times 10^5$ A m^{-1}.

The TDTR signal measured at the Pt side is a weighted average of the temperature profile through the Pt layer. In first order, the weighting function $\delta R(z)$ is the differential contribution of an infinitesimal layer at depth z to the change in reflectance per unit temperature change. We determine $\delta R(z)$ using a transfer matrix optical model assuming temperature coefficients of refractive index and extinction coefficient of Pt of $\partial n_{Pt}/\partial T = 2.6 \times 10^{-4}$ K^{-1} and $\partial k_{Pt}/\partial T = -3 \times 10^{-4}$ K^{-1} [47]. Due to the large diffusion constant of Cu electrons, relative variations in phonon temperature across the optical penetration depth of Cu are of the order of 1% and smaller. Therefore, we assume that the TDTR signal measured at the Cu side is proportional to the phonon temperature at the Cu surface.

[1] A. Hoffmann and S. D. Bader, Phys. Rev. Appl. **4**, 047001 (2015).
[2] G. Malinowski, F. Dalla Longa, J. H. H. Rietjens, P. V. Paluskar, R. Huijink, H. J. M. Swagten, and B. Koopmans, Nat. Phys. **4**, 855 (2008).
[3] A. Melnikov, I. Razdolski, T. O. Wehling, E. T. Papaioannou, V. Roddatis, P. Fumagalli, O. Aktsipetrov, A. I. Lichtenstein, and U. Bovensiepen, Phys. Rev. Lett. **107**, 076601 (2011).
[4] D. Rudolf, C. La-O-Vorakiat, M. Battiato, R. Adam, J. M. Shaw, E. Turgut, P. Maldonado, S. Mathias, P. Grychtol, H. T. Nembach *et al.*, Nat. Commun. **3**, 1037 (2012).
[5] T. Kampfrath, M. Battiato, P. Maldonado, G. Eilers, J. Notzold, S. Mahrlein, V. Zbarsky, F. Freimuth, Y. Mokrousov, S. Blugel *et al.*, Nat. Nano **8**, 256 (2013).
[6] C. von Korff Schmising, B. Pfau, M. Schneider, C. M. Günther, M. Giovannella, J. Perron, B. Vodungbo, L. Müller, F. Capotondi, E. Pedersoli *et al.*, Phys. Rev. Lett. **112**, 217203 (2014).
[7] A. J. Schellekens, K. C. Kuiper, R. R. J. C. de Wit, and B. Koopmans, Nat. Commun. **5**, 4333 (2014).
[8] A. Eschenlohr, M. Battiato, P. Maldonado, N. Pontius, T. Kachel, K. Holldack, R. Mitzner, A. Fhlisch, P. M. Oppeneer, and C. Stamm, Nat. Mater. **12**, 332 (2013).
[9] G.-M. Choi, B.-C. Min, K.-J. Lee, and D. G. Cahill, Nat. Commun. **5**, 4334 (2014).
[10] G.-M. Choi, C.-H. Moon, B.-C. Min, K.-J. Lee, and D. G. Cahill, Nat. Phys. **11**, 576 (2015).
[11] M. Battiato, K. Carva, and P. M. Oppeneer, Phys. Rev. Lett. **105**, 027203 (2010).
[12] G.-M. Choi and D. G. Cahill, Phys. Rev. B **90**, 214432 (2014).
[13] M. Hatami, G. E. W. Bauer, Q. Zhang, and P. J. Kelly, Phys. Rev. Lett. **99**, 066603 (2007).
[14] T. T. Heikkilä, M. Hatami, and G. E. W. Bauer, Phys. Rev. B **81**, 100408(R) (2010).
[15] F. K. Dejene, J. Flipse, G. E. W. Bauer, and B. J. van Wees, Nat. Phys. **9**, 636 (2013).
[16] J. Kimling, R. B. Wilson, K. Rott, J. Kimling, G. Reiss, and D. G. Cahill, Phys. Rev. B **91**, 144405 (2015).
[17] A. Slachter, F. L. Bakker, J.-P. Adam, and B. J. van Wees, Nat. Phys. **6**, 879 (2010).
[18] F. K. Dejene, J. Flipse, and B. J. van Wees, Phys. Rev. B **86**, 024436 (2012).
[19] W. S. Fann, R. Storz, H. W. K. Tom, and J. Bokor, Phys. Rev. B **46**, 13592 (1992).
[20] H.-S. Rhie, H. A. Dürr, and W. Eberhardt, Phys. Rev. Lett. **90**, 247201 (2003).
[21] V. P. Zhukov, E. V. Chulkov, and P. M. Echenique, Phys. Rev. B **73**, 125105 (2006).
[22] M. Battiato, K. Carva, and P. M. Oppeneer, Phys. Rev. B **86**, 024404 (2012).
[23] G. E. W. Bauer, E. Saitoh, and B. J. van Wees, Nat. Mater. **11**, 391 (2012).
[24] C. Illg, M. Haag, and M. Fähnle, Phys. Rev. B **88**, 214404 (2013).
[25] T. Valet and A. Fert, Phys. Rev. B **48**, 7099 (1993).
[26] A. Slachter, F. L. Bakker, and B. J. van Wees, Phys. Rev. B **84**, 174408 (2011).
[27] J. Kimling, J. Kimling, R. B. Wilson, B. Hebler, M. Albrecht, and D. G. Cahill, Phys. Rev. B **90**, 224408 (2014).
[28] W. M. Saslow, Phys. Rev. B **76**, 184434 (2007).
[29] G.-M. Choi, R. B. Wilson, and D. G. Cahill, Phys. Rev. B **89**, 064307 (2014).
[30] H. Nguyen, W. P. Jr., and J. Bass, J. Magn. Magn. Mater. **361**, 30 (2014).
[31] J. Kimling, K. Nielsch, K. Rott, and G. Reiss, Phys. Rev. B **87**, 134406 (2013).
[32] M. J. Verstraete, J. Phys.: Condens. Matter **25**, 136001 (2013).
[33] A. B. Schmidt, M. Pickel, M. Donath, P. Buczek, A. Ernst, V. P. Zhukov, P. M. Echenique, L. M. Sandratskii, E. V. Chulkov, and M. Weinelt, Phys. Rev. Lett. **105**, 197401 (2010).
[34] K.-i. Uchida, H. Adachi, T. Ota, H. Nakayama, S. Maekawa, and E. Saitoh, Appl. Phys. Lett. **97**, 172505 (2010).

[35] J. Xiao, G. E. W. Bauer, K.-c. Uchida, E. Saitoh, and S. Maekawa, Phys. Rev. B **81**, 214418 (2010).
[36] S. M. Rezende, R. L. Rodríguez-Suárez, R. O. Cunha, A. R. Rodrigues, F. L. A. Machado, G. A. Fonseca Guerra, J. C. Lopez Ortiz, and A. Azevedo, Phys. Rev. B **89**, 014416 (2014).
[37] M. Agrawal, V. I. Vasyuchka, A. A. Serga, A. Kirihara, P. Pirro, T. Langner, M. B. Jungfleisch, A. V. Chumak, E. T. Papaioannou, and B. Hillebrands, Phys. Rev. B **89**, 224414 (2014).
[38] A. Kehlberger, U. Ritzmann, D. Hinzke, E.-J. Guo, J. Cramer, G. Jakob, M. C. Onbasli, D. H. Kim, C. A. Ross, M. B. Jungfleisch *et al.*, Phys. Rev. Lett. **115**, 096602 (2015).
[39] J.-C. Le Breton, S. Sharma, H. Saito, S. Yuasa, and R. Jansen, Nature (London) **475**, 82 (2011).
[40] J. C. Leutenantsmeyer, M. Walter, V. Zbarsky, M. Münzenberg, R. Gareev, K. Rott, A. Thomas, G. Reiss, P. Peretzki, H. Schuhmann *et al.*, SPIN **03**, 1350002 (2013).
[41] W. Wang and D. G. Cahill, Phys. Rev. Lett. **109**, 175503 (2012).
[42] G. Tas and H. J. Maris, Phys. Rev. B **49**, 15046 (1994).
[43] A. P. Caffrey, P. E. Hopkins, J. M. Klopf, and P. M. Norris, Micro. Thermophys. Eng. **9**, 365 (2005).
[44] A. Brataas, A. D. Kent, and H. Ohno, Nat. Mater. **11**, 372 (2012).
[45] M. Zwierzycki, Y. Tserkovnyak, P. J. Kelly, A. Brataas, and G. E. W. Bauer, Phys. Rev. B **71**, 064420 (2005).
[46] Z. Lin, L. V. Zhigilei, and V. Celli, Phys. Rev. B **77**, 075133 (2008).
[47] R. B. Wilson, B. A. Apgar, L. W. Martin, and D. G. Cahill, Opt. Express **20**, 28829 (2012).